



Passive ground-based remote sensing of radiation fog

Heather Guy^{1,2}, David D. Turner³, Von P. Walden⁴, Ian M. Brooks², and Ryan R. Neely^{1,2}

¹National Centre for Atmospheric Science, Leeds, U.K.

²School of Earth and Environment, University of Leeds, Leeds, U.K.

³Global Systems Laboratory, National Oceanic and Atmospheric Administration, Boulder, CO, USA

⁴Department of Civil and Environmental Engineering, Laboratory for Atmospheric Research, Washington State University, Pullman, WA, USA

Correspondence: Heather Guy (heather.guy@ncas.ac.uk)

Abstract. Accurate boundary layer temperature and humidity profiles are crucial for successful forecasting of fog, and accurate retrievals of liquid water path are important for understanding the climatological significance of fog. Passive ground-based remote sensing systems such as microwave radiometers (MWRs) that have multiple channels between 22-31 GHz and 51-59 GHz, and infrared spectrometers such as the Atmospheric Emitted Radiance Interferometer (AERI) which measures spectrally resolved infrared radiation (3.3 to 19.2 μm) can retrieve both thermodynamic profiles and liquid water path. Both instruments are capable of long-term unattended operation and have the potential to support operational forecasting. Here we compare physical retrievals of boundary layer thermodynamic profiles and liquid water path during 13 cases of supercooled radiation fog from a MWR and an AERI collocated in central Greenland. We compare both sets of retrievals to in-situ measurements from radiosondes and surface-based temperature and humidity sensors. The retrievals based on AERI observations accurately capture shallow surface-based temperature inversions (0-10 m a.g.l) with lapse rates of up to $-1.2^\circ\text{C m}^{-1}$, whereas the strength of the surface-based temperature inversions retrieved from MWR observations are uncorrelated with in-situ measurements. For all but one case study, the retrievals based on AERI observations detect fog onset (defined by a threshold in liquid water path) earlier than those based on MWR observations by up to 4 hours. We propose that due to the high sensitivity of the AERI instrument to near-surface temperature and small changes in liquid water path, the AERI (or an equivalent infrared spectrometer) could be a useful instrument for improving fog monitoring and nowcasting.

1 Introduction

The socioeconomic and climatological impacts of fog are far-reaching. The reduction in visibility associated with fog disrupts transportation, resulting in economic losses equivalent to those associated with tornadoes and severe storms (Gultepe et al., 2007). Poor visibility due to fog is the most impactful extreme weather event in Arctic maritime operations (Panahi et al., 2020) and the second largest contributor to weather related accidents in aviation after adverse winds (Gultepe et al., 2019). Supercooled fog is particularly impactful since the collision of supercooled liquid droplets with a cold surface can result in the formation of rime or glaze ice. The build-up of ice can damage structures and power transmission lines (Ducloux and Nygaard, 2018) and presents an additional safety hazard in both shipping and aviation (Cao et al., 2018; Panahi et al., 2020),



making accurate forecasts of supercooled fog critical for risk mitigation. From a climatological perspective, fog is an important
25 moisture source, particularly in arid regions, (e.g. Hachfeld et al., 2000), and impacts the surface energy budget by modifying
radiant and turbulent energy transfer (Shupe and Intrieri, 2004; Beiderwieden et al., 2007; Anber et al., 2015). The hydrological
and radiative impacts of fog are both directly related to fog duration and liquid water content, and so accurate monitoring of
fog liquid water content is vital for understanding the role of fog in local climate and hydrological cycles.

Fog forms when the near-surface air reaches saturation resulting in the formation of liquid water droplets on condensation
30 nuclei (e.g. Oke, 2002). The air can reach saturation either through cooling until it reaches the dew point or through a moistening
process such as the evaporation of surface water/drizzle or moist air advection (Gultepe et al., 2007). The cooling of air near
the surface can result from advection (either cold air advection or the advection of a warm air mass over a cooler surface),
through orographic effects (i.e. the adiabatic cooling of air rising over topography, or cold air pooling in valleys) or through
direct radiative cooling of the surface. Fogs that primarily form through radiative cooling of the surface are known as radiation
35 fogs and commonly form on clear evenings with light winds - where the net surface cooling is maximised through the reduction
of direct solar heating and limited turbulent mixing of heat downward to the surface (e.g. Savijärvi, 2006). Due to the rapid
cooling of the surface, the formation of radiation fog is associated with a surface temperature inversion, which can be extremely
shallow, with most of the inversion often developing in the lowest 10 m above the surface (Hudson and Brandt, 2005; Price,
2011; Izett et al., 2019).

The onset of radiation fog in numerical weather prediction (NWP) models is particularly sensitive to the initial thermody-
40 namic structure of the boundary layer (Steenefeld et al., 2014). Accurate representation of boundary layer structure, particularly
temperature and humidity profiles in the lowest 1 km a.g.l and the development of the surface-based temperature inversion, is
thus crucial for forecasting radiation fog (Steenefeld et al., 2014; Gultepe et al., 2007; Bergot et al., 2007; Tardif, 2007); how-
ever, NWP models often fail to reproduce the strong but shallow gradients associated with it (Martinet et al., 2020; Westerhuis
45 and Fuhrer, 2021).

The assimilation of boundary layer thermodynamic profile measurements is one possibility for improving NWP forecasts of
radiation fog. However, making continuous high-resolution observations of temperature and humidity profiles is challenging.
Despite improvements in recent years, satellite retrievals of boundary layer profiles and fog characteristics remain insufficient
due to their coarse vertical resolution (> 1 km) and poor spatial coverage (Wulfmeyer et al., 2015; Wu et al., 2015; Wilcox,
50 2017; Yi et al., 2019). Surface-based in-situ measurements are limited by a maximum height (usually less than 50 m), while
radiosonde profiles are spatially and temporally sparse and resource intensive, and the development of a coordinated unmanned
aerial system profiling platform is still in its infancy (Jacob et al., 2018; McFarquhar et al., 2020). Active ground-based remote
sensors, such as differential absorption lidars (DIALs), can produce accurate thermodynamic profiles with a high temporal
resolution, but have a typical lowest range gate of greater than 100 m, making them unsuitable for fog monitoring (Newsom
55 et al., 2020; Stillwell et al., 2020; Turner and Lohnert, 2021).

In addition to thermodynamic profiles, accurate monitoring of liquid water content is important to understand the climato-
logical and hydrological impacts of fog. One metric to describe the liquid water content is fog liquid water path (LWP), defined
as the integral of liquid water content over the depth of the fog layer. LWP is directly related to visibility; for example, given a



homogeneous, mono-disperse fog with a depth of 100 m and a uniform droplet effective radius of $10 \mu\text{m}$, increasing the LWP
60 from 10 g m^{-2} to 20 g m^{-2} corresponds to a reduction in horizontal visibility from 200 to 100 m (assuming a visible contrast
threshold of 0.05; Bendix, 1995), highlighting the importance of accurate LWP retrievals for visibility nowcasting. The LWP
of thin fogs ($\text{LWP} < 40 \text{ g m}^{-2}$) is important from a climatological perspective because both longwave and shortwave surface
radiative fluxes become extremely sensitive to small changes in LWP (Turner et al., 2007a). Although thin liquid clouds and
fogs are common globally (Turner et al., 2007a), they are especially important in the Arctic where they dominate cloud radiative
65 forcing of the surface (Shupe and Intrieri, 2004; Miller et al., 2015). Cloud LWP was a critical control on the exceptional
Greenland Ice Sheet melt event of 2012; at the highest point on the ice sheet, a change in cloud LWP by $\pm 20 \text{ g m}^{-2}$ from the
observed value of $\sim 25 \text{ g m}^{-2}$ would have been sufficient to prevent surface melt (Bennartz et al., 2013).

Ground-based microwave radiometers (MWRs) are passive sensors that typically measure downwelling radiation at 22-31
70 GHz and 51-58 GHz in 14 to 35 different spectral channels and are sensitive to the temperature and water vapour profile in the
lowest 6 km of the atmosphere (Löhnert and Maier, 2012; Blumberg et al., 2015). Because MWRs can retrieve continuous (< 10 s)
boundary layer temperature and humidity profiles as well as LWP under both clear skies and non-precipitating clouds,
they are frequently used for fog monitoring (e.g. Gultepe et al., 2009; Wærsted et al., 2017; Temimi et al., 2020; Martinet
et al., 2020). Recent studies have demonstrated that the assimilation of MWR brightness temperatures into NWP models has
the potential to improve forecasts of stable boundary layers and fog by correcting errors in the temperature profile in the lowest
75 500 m above the surface (Martinet et al., 2017, 2020). The success of these trials contributed to EUMETNET's recent decision
to establish a homogeneous European network of MWRs by 2023 (Illingworth et al., 2019; Rüfenacht et al., 2021).

Despite the promise of MWRs to improve fog forecasts, the maximum vertical resolution of boundary layer temperature
profile retrievals (50 m at the surface decreasing to 1.7 km at 1 km a.g.l; Rose et al., 2005; Cadeddu et al., 2013) is insufficient to
resolve the shallow surface-based temperature inversions that often portend the onset of radiation fog (Price, 2011; Izett et al.,
80 2019). Although combining the MWR with active remote sensing instruments such as DIALs or Radio Acoustic Sounding
Systems (RASS) can improve the vertical resolution of the temperature profile retrievals in the lowest 2 km of the atmosphere,
these improvements do not extend down to the lowest 100 m a.g.l due to the height of the lowest range gate of the active
remote sensing instruments (Turner and Lohnert, 2021; Djalalova et al., 2021). In addition, large absolute uncertainties in LWP
retrievals from the MWR ($\pm 12\text{-}25 \text{ g m}^{-2}$) result in large errors during thin fog ($\text{LWP} < 40 \text{ g m}^{-2}$; Turner, 2007b).

Another passive remote sensing instrument, the Atmospheric Emitted Radiance Interferometer (AERI, Knuteson et al.,
2004a) has greater sensitivity than MWRs to both changes in near surface (< 1 km) thermodynamic profiles (Blumberg et al.,
2015; Turner and Lohnert, 2021) and small changes in LWP (for $\text{LWP} < 40 \text{ g m}^{-2}$, Turner, 2007b). The AERI measures spec-
trally resolved downwelling infrared radiation between 3.3 and $19.2 \mu\text{m}$. Because of the higher opacity at infrared wavelengths
relative to the optical depths spanned by the MWR, the AERI can detect changes in the boundary layer thermodynamic profile
90 at a finer vertical resolution and with greater accuracy than the MWR (Blumberg et al., 2015; Turner and Lohnert, 2021). The
primary disadvantage is that the AERI is not sensitive to atmospheric properties above a cloud with a $\text{LWP} > \sim 40 \text{ g m}^{-2}$, for
which the cloud is nearly opaque in the infrared. This means that retrievals of thermodynamic profiles above optically thick
clouds are not possible, and retrievals below them are only possible if the cloud temperature and height are well characterised.



Although several studies have compared the performance of AERI and MWR retrievals of thermodynamic profiles and LWP
95 under different conditions (Blumberg et al., 2015; Turner, 2007b; Löhnert et al., 2009; Turner and Löhnert, 2021), none of
these studies have included cases of fog. Fog is distinct from ‘cloudy scenes’ in general because the LWP and changes in the
thermodynamic profile that are relevant for fog development and life-time are concentrated in the lowest layers (< 100 m)
above the surface. The goal of this study is to compare the performance of thermodynamic and LWP retrievals based on MWR
and AERI observations during fog events, with an emphasis on those aspects that are crucial for making accurate forecasts
100 and understanding the climatic impact of fog: The representation of the thermodynamic profile in the lowest 1 km a.g.l, the
detection of shallow surface based temperature inversions, and accurate measurements of small changes in fog LWP.

We take advantage of the collocation of a MWR and an AERI alongside a large suite of supplementary instruments for
monitoring atmospheric properties at Summit Station (Summit), in the centre of the Greenland Ice Sheet (Shupe et al., 2013).
The surface air temperature at Summit approaches 0°C only in exceptional circumstances (NSIDC, 2021), and supercooled
105 radiation fog is common, occurring over 10% of the time in the summer (Cox et al., 2019). Summer-time radiation fog in
central Greenland is particularly impactful because it forms during the coldest part of the day and has a net warming effect
at the surface, effectively dampening the diurnal temperature cycle with the potential to precondition the ice sheet surface for
melt (Solomon et al., 2017; Cox et al., 2019). Aviation operations at Summit are also frequently disrupted by the low visibility.

Using a consistent physical retrieval algorithm for both instruments, we compare the suitability of the MWR and the AERI
110 for retrieving near surface thermodynamic profiles and LWP during super-cooled radiation fog events at Summit in the summer
of 2019. We evaluate the retrieved thermodynamic profiles against radiosonde profiles and in-situ temperature and humidity
measurements and assess the ability of each set of retrievals to detect the increase in LWP associated with the onset of fog.
Henceforth in this study ‘fog’ will specifically pertain to supercooled radiation fog unless otherwise specified.

2 Methods

115 2.1 Measurement site and instrumentation

The Integrated Characterization of Energy, Clouds, Atmospheric state and Precipitation at Summit (ICECAPS) project col-
lected continuous observations of the atmosphere above Summit from 2010 to 2021 (Shupe et al., 2013). At the highest point
of the Greenland Ice Sheet (-38.45 E, 72.58 N, 3250 m a.s.l.), the atmosphere above Summit is extremely dry and temperatures
are rarely above freezing (Shupe et al., 2013). The ice sheet surface is homogeneous in all directions, so that the atmospheric
120 conditions at Summit are minimally influenced by local topography. During the summer (JJAS), freezing fog (defined as fog
that reduces visibility to less than 1,000 m) was reported by on-site observers 10 % of the time (2010-2020). These fogs can
occur when surface temperatures are as low as -35°C and almost always contain supercooled liquid droplets (Cox et al., 2019),
presumably due to a lack of ice nucleating particles (near surface aerosol concentrations at Summit are exceptionally low, Guy
et al., 2021). The applicability of the results of this study to other (less extreme) environments is discussed in section 4.

125 The Aerosol Cloud Experiment (ACE) was added to the ICECAPS project in 2019 and included the addition of temperature
and humidity sensors and sonic anemometers at four levels on a 15 m tower for high resolution monitoring of the near-surface

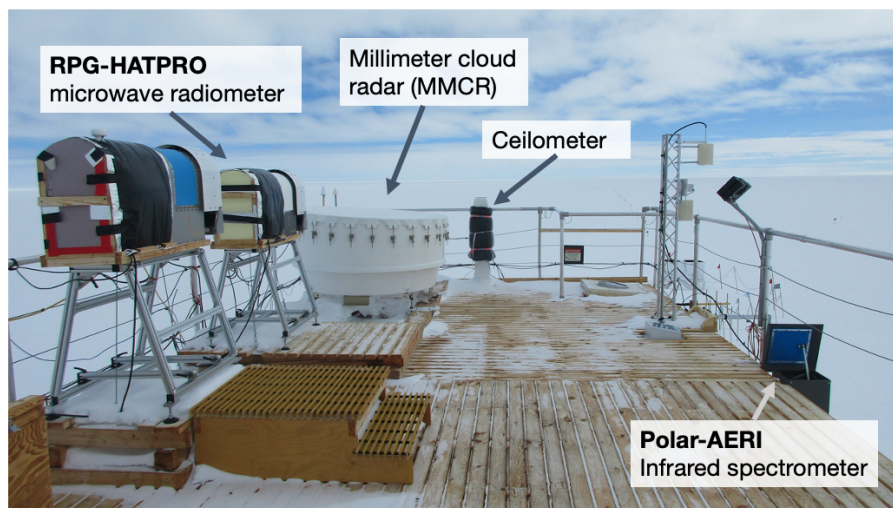


Figure 1. Key ICECAPS-ACE instrumentation at Summit Station (photographed by the author, 16 May 2019).

turbulent and thermodynamic structure (Guy et al., 2021). For this study, we focus on fog events during the summer of 2019 whilst the multi-level temperature and humidity data from the tower are available. Figure 1 shows the experimental setup of the MWR and AERI at Summit, and Table 1 provides details of all the ICECAPS-ACE instrumentation used in this study.

130 We use the tower mounted temperature and humidity probes (Vaisala HMP155, installed in aspirated shields) as ‘true’ reference points to assess the performance of the surface temperature retrievals from the MWR and AERI. The instrument uncertainty for the HMP155 is $< \pm 2.5\%$ relative humidity and $< \pm 0.3^\circ\text{C}$. For this study, we define the ‘surface’ as the height of the raised platform photographed in Fig. 1, where both the AERI and MWR windows are situated. This surface is aligned with the HMP155 sensor mounted on the tower at 4 m above the snow surface; measurements from this sensor are henceforth
135 referred to as surface temperature and humidity. Measurements from the HMP155 sensor located 10 m higher on the tower are compared to the 10 m thermodynamic retrievals. The same height adjustment is applied to the radiosonde profiles prior to comparison (which are launched approximately 3 m below the platform ‘surface’, or 1 m above the snow surface). The uncertainty in the radiosonde measurements is $\pm 4\%$ relative humidity and $\pm 0.3^\circ\text{C}$ (Jensen et al., 2016).

2.1.1 The AERI

140 The polar AERI (PAERI) at Summit was designed and manufactured by personnel at the Space Science and Engineering Center (SSEC) at the University of Wisconsin-Madison, and is one of the original AERIs developed for the US Department of Energy’s Atmospheric Radiation Measurement (ARM) program (Turner et al., 2016). It was built and calibrated according to specifications in Knuteson et al. (2004a) and adheres to the performance requirements of radiometric calibration ($< 1\%$, 3σ , of ambient radiance) and spectral calibration (1.5 ppm , 1σ) as explained by Knuteson et al. (2004b). The PAERI measures
145 downwelling spectral infrared radiance between 3 and $19\ \mu\text{m}$ at an unapodized spectral resolution of about $0.48\ \text{cm}^{-1}$ (see



Table 1. Overview of instrumentation used in this study. All instruments were installed at Summit as part of the ICECAPS project (Shupe et al., 2013) or ICECAPS-ACE project (Guy et al., 2021).

Title	Instrument	Key specifications	References
PAERI	Polar Atmospheric Emitted Radiance Interferometer	530-3,000 cm^{-1} (3-19 μm), 1 cm^{-1} res. < 1-min time res.	(Knuteson et al., 2004a) (Walden et al., 2005)
HATPRO MWR	RGP Humidity and Temperature Profiler, microwave radiometer	Frequencies: 7 channels 22-32 GHz, 7 channels 51-58 GHz, 2-4 s time resolution.	(Rose et al., 2005)
MMCR	Millimetre cloud radar	Ka band (35 GHz), 8-mm wavelength, 45 m vertical res. 2 s time res.	(Moran et al., 1998)
Ceilometer	Vaisala laser ceilometer CT25K	905 nm wavelength. 15 m vertical res., 15 s time res.	(Münkel et al., 2006)
POSS	Precipitation Occurrence Sensor System	X-band radar (10.5 GHz) 1-min time res. Single volume near surface.	(Sheppard and Joe, 2008)
Temperature and humidity probes	Vaisala HMP155, aspirated	1-min averages at 0 m and 10 m.	(Guy et al., 2020)
Radiosondes	Vaisala RS41-SG	Launched at 12 and 00 UTC daily.	(Jensen et al., 2016)

Table 3 from Knuteson et al., 2004a). The PAERI operates on a continuous measurement schedule where it obtains views of the hot and ambient calibration sources, followed by eight consecutive views of the sky at zenith. The sequence is repeated so that each set of eight sky views is bracketed in time by views of both calibration sources; these sources are then used to calibrate the eight sky views. Each of the spectral measurements is a ‘co-addition’ of six interferometric scans. Each complete, calibrated measurement sequence takes approximately 3 minutes with the sky views separated by approximately 15-20 s. This yields more than 3300 infrared spectra each day. Quality control is then applied to each of the spectra by eliminating those that have instrument parameters outside of acceptable limits; the acceptable limits were set by SSEC personnel. The important instrument parameters are the responsivities and noise-equivalent radiances of the hot blackbody calibration source measured by both of the PAERI detectors (InSb and MCT), plus the current and temperature of the Stirling cooler that maintains the detectors at 77 K. In actuality, the instrument responsivities are a very sensitive indicator of the PAERI’s health, and most unusable spectra are eliminated by low responsivity associated with small amounts of snow on the PAERI scene mirror. Finally, the remaining



calibrated sky views are subjected to noise filtering using the technique described by Antonelli et al. (2004) and Turner et al. (2006).

2.1.2 The MWR

160 The MWR at Summit, a Humidity and Temperature Profiler (HATPRO) from Radiometer Physics GmbH, observed down-
welling radiation in all 14 channels simultaneously every 4 seconds (see table 2 for channel details). After collecting 600
zenith views, the HATPRO collected elevation scans at 5.4, 10.2, 16.2, 19.2, 23.4, 30.0, and 42.0 on either side of zenith. These
elevation scans were used to both evaluate and update the calibration accuracy of the K-band channels (i.e., the low opacity
channels between 22 and 32 GHz) using the tip-curve technique (Han, 2000). The more opaque V-band channels (i.e., in the 51
165 to 58 GHz band) were calibrated twice yearly using an external liquid nitrogen target; the most recent calibration used for this
analysis was performed on 01 May 2019. Both the tip curves and the liquid nitrogen views are used to determine the effective
temperature of the internal noise diode, which is used regularly when viewing the internal blackbody to establish two different
reference values (i.e., one ambient blackbody view with the noise diode off, and one 'hot' blackbody view with the noise diode
on). These internal blackbody views, which are done every minute, are used to continually update the gain of the radiometer
170 and convert the observed signal to brightness temperature, following the calibration principles outlined in Liljegren (2000).

However, since the liquid nitrogen calibrations are performed infrequently, any drift in the effective temperature of the
noise diode in the V-band channels will result in a calibration bias. Using a radiative transfer model (the monochromatic
MonoRTM, Clough et al., 2005) with radiosonde profiles as input, we have determined a brightness temperature offset that is
subtracted from the observed brightness temperatures. The bias correction, and the impact of not applying this correction prior
175 to performing the thermodynamic retrievals are discussed in Appendix A.

2.2 Case study identification

To identify case studies of radiation fog under otherwise clear skies, we only considered times when there were no clouds
detected by the MMCR, which has a lowest range gate close to 200 m a.g.l and is therefore insensitive to fog, and when
there was no precipitation detected by the POSS. Of the times that met these criteria, fog was provisionally identified when
180 the 962 cm^{-1} downwelling radiance measured by the AERI was greater than a threshold of 1.7 RU (radiance units, $1\text{RU} = 1$
 $\text{mW m}^{-2}\text{ sr}^{-1}\text{ cm}^{-1}$). In the extremely dry atmosphere over Summit, clear-sky transmittance is almost unity at 962 cm^{-1} , so
this micro-window is particularly sensitive to the presence of clouds (e.g. Cox et al., 2012). The threshold value of 1.7 RU is
three standard deviations above the mean 962 cm^{-1} radiance during 236 verified clear sky hours between June and Sept 2019,
and therefore identifies when the AERI window was obscured by cloud/fog. Ambiguous cases when there was evidence that
185 something other than fog may have caused the 962 cm^{-1} radiance increase, such as clear sky ice crystal precipitation, high
cirrus clouds, or the plume from the station generator, were removed based on the observer log and photographs. Table 3 details
the 13 cases that met the criteria above and were selected for the intercomparison. In each case, the fog forms in late evening
or early morning and usually dissipates by midday as is characteristic of radiation fog (Fig. 2).



Table 2. Centre frequencies, assumed noise level, whether the elevation scans for the frequency are included in the observation vector, and the bias offset applied to the observations for the HATPRO MWR at Summit.

Frequency GHz	Noise Level K	Used in Elev. Scan	Bias Offset K
22.24	0.30	No	0.23
23.04	0.30	No	0.08
23.84	0.30	No	0.09
25.44	0.30	No	0.00
26.24	0.30	No	0.12
27.84	0.30	No	0.17
31.40	0.30	No	0.15
51.26	0.80	No	2.02
52.28	0.80	No	2.15
53.86	0.50	No	2.03
54.94	0.30	Yes	-0.45
56.66	0.30	Yes	-0.32
57.30	0.25	Yes	-0.12
58.00	0.25	Yes	-0.11

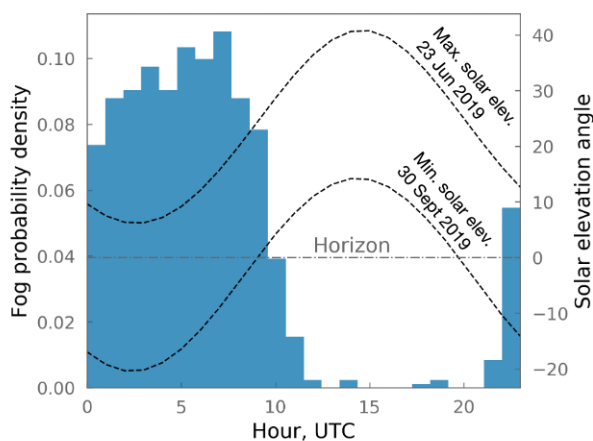


Figure 2. Diurnal distribution of fog during the summer 2019 case studies listed in Table 3 (blue bars). Black dashed lines show the maximum and minimum solar elevation angles (Jun – Sept 2019). Local time at Summit is UTC-3 h.



Table 3. Details of the 13 radiation fog cases used in this study including mean temperatures (T) and water vapor mixing ratios (wv). Note that the minimum visibility comes from observer reports at 00, 12 and 18 UTC and may not represent the minimum visibility outside of these times. A value of 9999 is reported if horizontal visibility is not impeded. Local time is UTC-3h.

ID	Case start Date Time. UTC, 2019	Case end Date Time UTC, 2019	Duration (h)	Mean surface T (°C)	Mean surface wv (g kg ⁻¹)	Min visibility (observer log, m)
1	08 Jun 03:30	08 Jun 10:00	6.5	-17	1.3	4,800
2	12 Jun 02:00	12 Jun 10:30	8.5	-9.6	2.5	4,800
3	13 Jul 22:00	14 Jul 07:00	9.0	-20	0.96	1,600
4	15 Jul 21:00	16 Jul 11:00	14	-18	1.2	400
5	31 Jul 22:25	01 Aug 08:30	10	-10	2.4	400
6	01 Aug 18:00	02 Aug 15:00	21	-10	2.3	800
7	03 Aug 19:00	04 Aug 09:00	14	-14	1.7	9999
8	04 Aug 21:30	05 Aug 12:00	15	-17	1.3	400
9	05 Aug 23:00	06 Aug 10:00	11	-20	0.91	1,600
10	09 Aug 19:00	10 Aug 04:00	9.0	-16	1.4	1,600
11	14 Aug 23:00	15 Aug 10:00	11	-26	0.54	3,200
12	05 Sep 02:00	05 Sep 12:00	10	-25	0.59	400
13	30 Sep 02:00	30 Sep 12:00	10	-27	0.47	4,800

2.3 Retrieval methodology

190 We retrieve boundary layer thermodynamic profiles (temperature, T, and water vapor mixing ratio, wv) and LWP at a 5-min
 temporal resolution using the TROPoe iterative optimal estimation physical retrieval algorithm that is detailed in Turner and
 Lohnert (2021) and Turner and Blumberg (2019). TROPoe uses a forward model to calculate the observation vector from the
 current state vector, where the state vector is the retrieved thermodynamic profile and LWP, and the observation vector is the
 downwelling radiance observed by either the polar AERI or HATPRO MWR. Surface meteorological measurements are not
 195 included in the observation vector to allow for their use as an independent validation measurement; the impact of including
 surface measurements in the retrievals is discussed in Appendix B. Note that the observation vector from the MWR includes
 data from the elevation scans at 10.2, 16.2, and 19.2 degrees for the four most opaque V-band channels; including elevation
 scans in the retrieval has been shown to increase the accuracy of the retrieved temperature profile (Crewell and Lohnert, 2007).
 The forward models are line-by-line radiative transfer models; the LBLRTM version 12.1 (Clough and Iacono, 1995) simulates
 200 the AERI spectral radiances, and the monochromatic MonoRTM (Clough et al., 2005) simulates the MWR radiances. Note that
 the latter uses the improved temperature-dependent liquid water absorption coefficients (Turner et al., 2016). The state vector is
 incrementally adjusted to minimise the difference between the forward model calculation and the observation vector until the



change between successive iterations is less than the uncertainty in the current state vector (Rodgers, 2000). We run TROPoe in two physically consistent configurations; once using only the PAERI radiances as the observation vector (as in Turner and
205 Löhnert, 2014, henceforth named AERIOe) and once using only the microwave brightness temperature observations from the HATPRO MWR (as in Löhnert et al., 2009, henceforth named MWRoe).

Thermodynamic retrieval from passive spectral radiance observations is an ill-posed problem, hence the optimal-estimation retrieval is necessarily constrained by an a priori probability density function (the prior) that provides the first guess state vector that stabilises the retrieval (Turner and Löhnert, 2014). Typically, a location specific prior can be derived from a database of
210 historical observations (i.e. from radiosonde profiles) at or near the location of interest. The prior for Summit is computed from 1756 summer radiosonde launches (2010-2018). However, due to the rapid warming in the Arctic (e.g. Koenigk et al., 2020), this does not encapsulate the exceptionally warm and moist conditions at Summit during the summer of 2019 (NSIDC, 2019). To allow the retrievals more flexibility to account for the exceptional conditions, we have re-centered the prior using the mean of the three closest radiosondes to the retrieval date (whilst conserving relative humidity), and increased the wv variance in the
215 prior by a factor of four at the surface (decreasing to 0 by 1 km a.g.l).

Previous studies have used cloud base height (CBH) derived from a collocated ceilometer as an additional constraint on the retrieval which allows the retrieval of below-cloud thermodynamic profiles from the AERI in the presence of thick clouds (Turner et al., 2007a; Turner and Löhnert, 2014; Blumberg et al., 2015). Because we focus on radiation fogs under otherwise clear skies, which are, by definition, based at the surface, we initially assumed that the CBH is 5 m a.g.l in all cases. However,
220 large temperature biases (> 5 K) in the AERIOe retrievals during fog illustrated that the TROPoe is highly sensitive to the CBH assumption when using AERI data as an input (see section 3.1). For the final retrievals, we used CBH from the ceilometer to constrain the retrieval if the ceilometer detects a cloud base within 10 minutes of the retrieval time, or if the ceilometer reports obscured vertical visibility, then the detected vertical visibility height (Morris, 2016) is input as the CBH. If neither of these situations occurs, the CBH assumption defaults to 5 m a.g.l. The sensitivity of the retrievals to this choice is discussed further
225 in section 3.1.

The retrieval algorithm outputs 1σ uncertainties for all variables that incorporate the random error from the observations, the correlated error propagated from the prior, and the sensitivity of the forward model. Errors related to the CBH assumption or phase assumption (when only liquid water is considered) are not included, and we discuss these below in section 3.1 and section 4.

230 2.4 Evaluation metrics

To evaluate the two TROPoe retrieval configurations (AERIOe and MWRoe) we focus on three aspects that are crucial for making accurate fog forecasts with NWP models, for visibility nowcasting, and for understanding the climatic impact of fog:

1. Accurate representation of the structure of the temperature and humidity profile in the lowest 1 km a.g.l.
2. Detection of the presence and strength of shallow surface-based temperature inversions that typically portend the forma-
235 tion of radiation fog.



3. Detection of the initial increase in LWP that signifies the onset of fog and a reduction in horizontal visibility.

To evaluate the accuracy of the temperature and humidity profile retrievals in the lowest 1 km a.g.l, we assess the performance of the MWRoe and AERIOe against 16 coincident radiosonde profiles by evaluating the mean bias and spread between the radiosonde profiles (truth) and the retrievals. We use modified Taylor diagrams (Taylor, 2001; Turner and Löhnert, 2014) to
240 assess how well the retrieved profiles capture the shape of the true profiles by considering the Pearson's correlation coefficient and the ratio of the standard deviation of the retrieval to that of the truth profile. These results allow for a direct comparison with Blumberg et al. (2015) who compare MWRoe and AERIOe retrievals against a larger number of radiosonde profiles (127) in southwestern Germany (but only consider clear sky days or clouds with bases > 500 m a.g.l).

To evaluate the ability of each retrieval to detect the occurrence and strength of surface-based temperature inversions, we
245 compare the retrieved surface (0 m) and 10 m temperatures with measurements from in-situ temperature sensors (see section 2.1). We define the inversion 'strength' as the 10 m – 0 m temperature and evaluate the Pearson's correlation coefficients and root-mean-squared error (RMSE) between the retrieved values and the 'truth' (the in-situ temperature sensors). Klein et al. (2015) performed a similar analysis comparing the temperature difference between 10 and 100 m a.g.l. Although we are limited by a maximum sensor height on the tower, we expect the 10 m - 0 m temperature difference to be a good indicator of whether
250 the retrieval captures the surface-based temperature inversion since most of the inversion during radiation fog often occurs in the lowest 10 m a.g.l (Price, 2011; Izett et al., 2019).

Finally, in the absence of an independent method of determining LWP, we evaluate the ability of each retrieval to detect the initial increase in LWP associated with fog formation and visibility reduction by defining 'fog onset' as where the retrieved LWP minus 2σ uncertainty (which is directly computed by TROPoe) increases above 0.1 g m^{-2} for at least 10 minutes,
255 and then compare the difference in fog onset detection time between the MWRoe and the AERIOe for each case study. This methodology allows us to identify when each retrieval identifies a LWP that is above the measurement noise level, hence comparing the sensitivity of the two sets of retrievals to small increases in liquid water that can begin to reduce visibility and impact radiative energy fluxes at the surface.

3 Results

260 3.1 Retrieval performance and sensitivity to cloud base height assumption

All 2334 retrievals from both AERIOe and MWRoe converged, meaning that the retrieval algorithm was able to find a solution within the maximum number of iterations. The mean root mean squared error (RMSE) between the final forward model calculation and the observed PAERI radiance across all AERIOe retrievals was 0.54 ± 0.09 RU, which is of the order of the instrument noise level (Blumberg et al., 2015). For the MWRoe retrievals the mean RMSE between the final forward model
265 calculation and the MWR brightness temperatures was 0.38 ± 0.12 K, again within the instrument noise (Rose et al., 2005).

The AERIOe retrievals were very sensitive to the cloud base height (CBH) assumption. Because we are only considering cases of radiation fog under otherwise clear skies, the first iteration of retrievals assumed that, if liquid water was detected, the

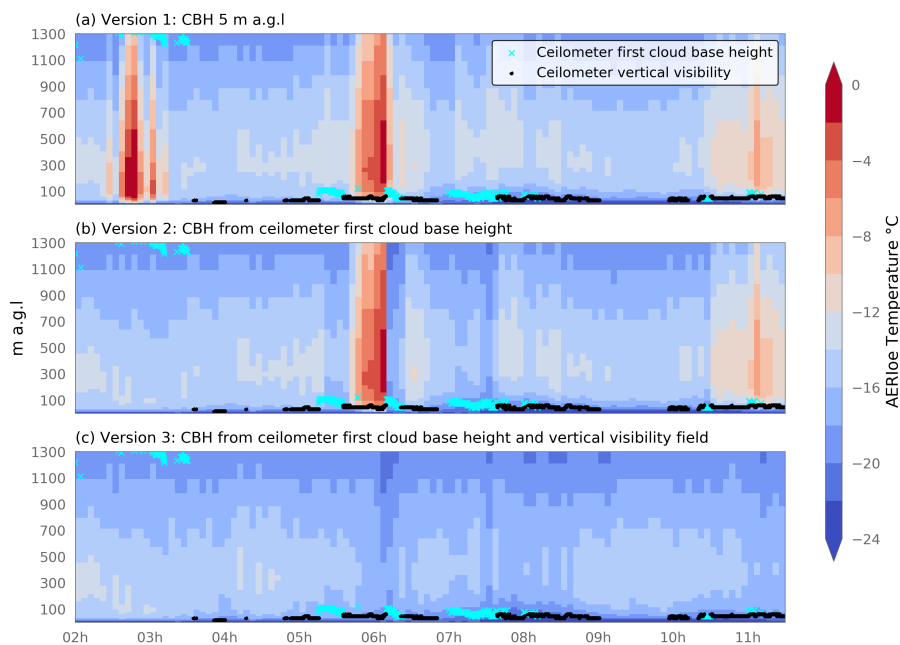


Figure 3. Temperature profiles during the 05 Sept case study from three iterations of the AERIoe retrieval using different CBH assumptions. The ceilometer first cloud base height field is overlaid as cyan crosses and the vertical visibility field is overlaid as black circles. (a) Assumed CBH was 5 m a.g.l any time LWP > 0, (b) assumed CBH was set to the ceilometer ‘first cloud base height’ if the ceilometer detected a cloud within the 10-mins centred on the retrieval time, otherwise 5 m a.g.l, (c) as in (b) except if the ceilometer reported ‘obscured’ the CBH was set equal to the ceilometer maximum vertical visibility field.

cloud base height was 5 m a.g.l, removing the requirement for additional instrumentation to detect CBH. Figure 3a demonstrates that under this assumption, the AERIoe retrieved unrealistic temperature profiles in some cases when the fog was optically thick (i.e. ceilometer is obscured), or when the ceilometer detected a cloud with a base close to 1,300 m a.g.l prior to the start of the fog event. The unrealistic temperature profiles manifest as exceptionally warm temperatures just above the surface, indicated by red colours in Fig. 3.

Previous AERIoe algorithms have used the ceilometer ‘first cloud base height’ field (an output of the Vaisala proprietary software) to estimate CBH (Turner and Löhnert, 2014; Blumberg et al., 2015). Using this assumption rather than simply assuming the CBH to be 5 m a.g.l reduced the temperature profile artifacts in some, but not all cases (fig. 3b). The ceilometer software also outputs a ‘vertical visibility’ field (described in Morris, 2016) when the extinction profile is such that the atmosphere is obscured but no distinct cloud base can be determined, as often happens in the case of thick fog. The remaining artifacts in the example case study occur when the ceilometer reports a vertical visibility value (Fig. 3b). When we used the vertical visibility field in addition to the ‘first cloud base height’ field to provide the CBH assumption in the AERIoe retrieval, the remaining artifacts were removed (Fig. 3c).



Even if the fog is reducing visibility at the surface, the ‘cloud base height’ is the height at which the fog becomes optically thick to the PAERI, which is similar to when it becomes optically thick for the ceilometer (which uses radiation in the near-infrared, 905 nm). Figure 3 shows that a difference in CBH of just 30 m can make a significant difference to the retrieval when the cloud is close to the surface, demonstrating that accurate CBH measurements are a necessary input to the AERIOe
285 for retrieving thermodynamic profiles in the presence of fog or near-surface clouds. In contrast, the MWRoe was not sensitive to the CBH assumption, because clouds are markedly more transparent and microwave frequencies. For the remainder of this study, all retrievals (AERIOe and MWRoe) derive CBH from both the ‘first cloud base height’ and ‘vertical visibility’ field of the ceilometer.

3.2 Performance of retrieved thermodynamic profiles in the lowest 1 km a.g.l

290 The AERIOe temperature profiles (0 - 1 km a.g.l) compared extremely well to the 16 radiosonde profiles considered, with a mean bias of -0.45°C and a mean RMSE of 1.0°C (Fig. 4a). The MWRoe temperature profiles exhibited a vertically consistent negative bias compared to the radiosonde profiles with an average value of -1.5°C and an average RMSE of 1.6°C (Fig. 4a). Although investigating the source of the negative bias in the MWRoe temperature profile is outside the scope of this study, such systematic biases can often be corrected for, and the similar spread in bias magnitude between the AERIOe and the
295 MWRoe temperature retrievals imply that the performance of the two sets of retrievals would be similar after an additional bias correction (Fig. 4a). For both sets of retrievals, the temperature RMSE is largest in the lowest 50 m a.g.l where it approaches 2.0°C (Fig. 4a).

For water vapor, the performance of the AERIOe and MWRoe retrievals compared to the radiosonde profiles was very similar (Fig. 4b). Neither set of retrievals exhibited a mean bias, and the RMSE of the AERIOe retrievals was slightly smaller than the
300 MWRoe up to 800 m a.g.l with a mean value of 0.38 g kg^{-1} (compared to 0.43 g kg^{-1} for the MWRoe).

Figures 4c and 4d show that both sets of temperature profile retrievals are better correlated with the radiosonde profiles ($r > 0.98$, Fig. 4c,) than the water vapor profile retrievals, which in some cases have correlation coefficients < 0.6 (Fig. 4d), but the spread in the standard deviation ratio is similar (0.9 - 1.2). The AERIOe retrievals (for both temperature and water vapor) have a similar spread in correlation coefficients and standard deviation ratios to the MWRoe retrievals, implying that the performance
305 of the two retrievals was comparable across this subset of profiles.

3.3 Characterisation of shallow surface-based inversions

The AERIOe temperature retrievals at 0 and 10 m a.g.l are equally well correlated with observations ($r = 0.99$, $\text{RMSE} = 1.1^{\circ}\text{C}$), implying that the AERIOe captures vertical temperature gradients in the lowest 10 m of the atmosphere well and retrieves surface temperatures consistently with high accuracy (Fig. 5). In comparison, the MWRoe retrievals perform worse than the
310 AERIOe at both heights, with $r = 0.86$, $\text{RMSE} = 4.1^{\circ}\text{C}$ at 0 m, and $r = 0.95$, $\text{RMSE} = 2.1^{\circ}\text{C}$ at 10 m (fig. 5). Notably, the performance of the MWRoe is worst at 0 m, where the MWRoe typically has a warm bias at colder temperatures (72% of the time when $T < -7^{\circ}\text{C}$) and a cold bias at warmer temperatures (93% of the time when $T > -7^{\circ}\text{C}$). This bias reduced at 10 m, implying that the temperature lapse rate between 0 and 10 m a.g.l is often incorrect in the MWRoe retrieval (Fig. 5).

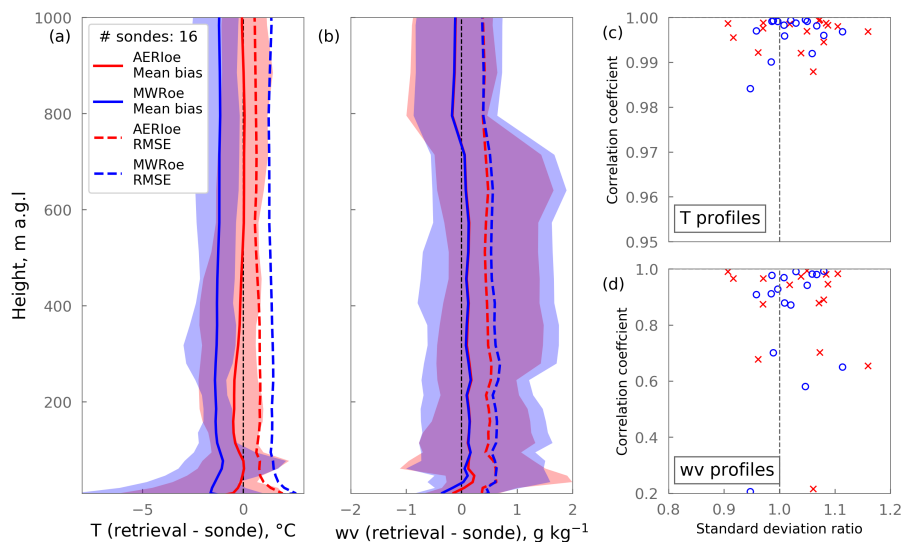


Figure 4. Comparison between retrieved thermodynamic profiles and the 16 coincident radiosonde profiles in the lowest 1 km a.g.l. (a) The temperature and (b) and water vapor bias (retrieval – radiosonde) for AERIoe retrievals (red) and MWRoe retrievals (blue), the solid line shows the mean bias and the shaded represents the range. Dashed lines show the root mean squared error (RMSE) (c) The temperature and (d) water vapor modified Taylor plots showing the relationship between the correlation coefficient and standard deviation ratio for each retrieval/radiosonde pair ([1,1] represents a perfect score) for the AERIoe retrievals (red) and the MWRoe retrievals (blue).

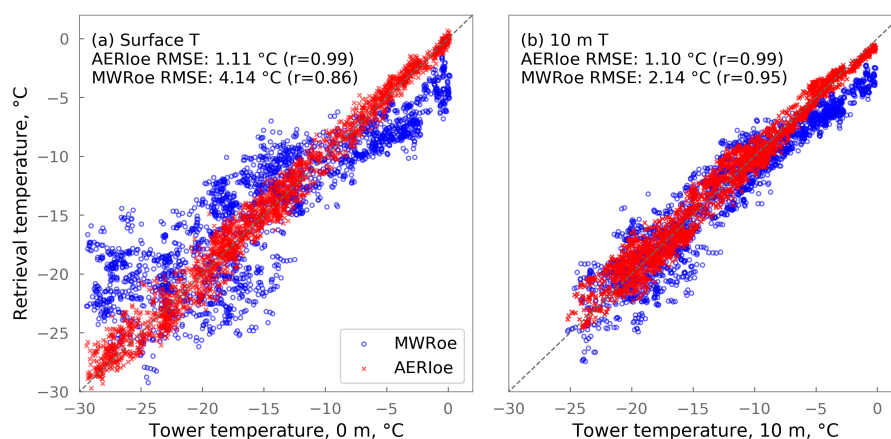


Figure 5. MWRoe (blue circles) and AERIoe (red crosses) retrieved temperature versus in-situ temperature measurements from tower mounted HMP155 probes at the surface (a) and 10 m (b). The dashed grey line represents perfect agreement. The Pearson’s correlation coefficient (r) and root mean squared error (RMSE) between each set of retrievals and the tower measurements are included on the figure.

Figure 6 shows the poor performance of the MWRoe in retrieving the 0-10 m temperature lapse rate by demonstrating that there is no correlation between the measured surface inversion strength (10 - 0 m T) and that retrieved by the MWRoe. In fact,

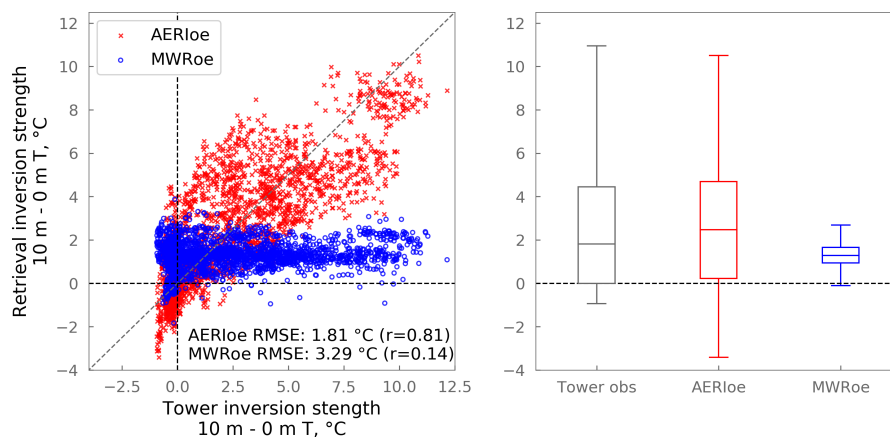


Figure 6. (a) Inversion strength (10 m – 0 m T) retrieved from the AERloe (red) and the MWRoe (blue) versus observations from the tower mounted HMP155 probes. The diagonal grey dashed line represents perfect agreement and the horizontal and vertical dashed black lines at 0°C delineate when a surface based temperature inversion is present (right quadrants) versus absent (left quadrants). (b) The distribution of inversion strength recorded by the tower observations, the AERloe, and the MWRoe.

in most cases the surface inversion strength retrieved by the MWRoe is $\sim 1^\circ\text{C}$, close to the surface inversion strength in the retrieval prior (0.7°C). This suggests that most of the information about the change in temperature between 0 and 10 m comes from the prior rather than the observations. In contrast, the AERloe surface inversion strength is well correlated with in-situ measurements ($r=0.81$) with a RMSE of 1.8°C (Fig. 6). Figure 6 demonstrates that the AERloe can accurately retrieve shallow surface temperature inversions with lapse rates of up to $-1.2^\circ\text{C m}^{-1}$.

The reason that the AERloe can accurately retrieve shallow surface-based temperature inversions but the MWRoe cannot is because the PAERI infrared radiance measurements theoretically contain much more information about the near-surface temperature profile than the MWR brightness temperatures (Blumberg et al., 2015). Figure 7 supports this, by illustrating that the degrees of freedom for signal for temperature from the AERloe retrievals is greater than that from the MWRoe retrievals, especially at the surface. The degrees of freedom for signal is a measure of the number of independent pieces of information from the observation vector that the retrieval used to generate the solution (Rodgers, 2000). Figure 7 shows that the AERloe has around six times as much information about the surface temperature than the MWRoe, and twice as much at 10 m.

3.4 LWP retrievals and the detection of fog onset

The LWP retrievals from the AERloe and MWRoe were well correlated ($r=0.88$) and fell within $\pm 5 \text{ g m}^{-2}$ of each other in $\sim 90\%$ of all retrievals, however on occasions there were discrepancies of up to 10 g m^{-2} (Fig. 8), which can be equivalent to significant differences in horizontal visibility and net surface radiative forcing (see examples in section 1).

Although we do not have an independent measure of the ‘true’ LWP, Fig. 9 illustrates the difference in sensitivity of the MWRoe and the AERloe to LWP as a function of LWP magnitude. The PAERI radiance observations are very sensitive to

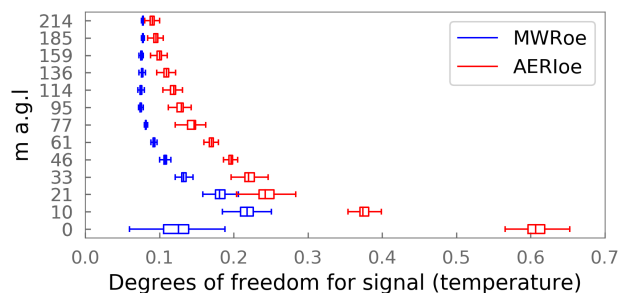


Figure 7. Distribution of the degrees of freedom for signal near the surface for all temperature retrievals from the MWRoe (blue) and AERloe (red).

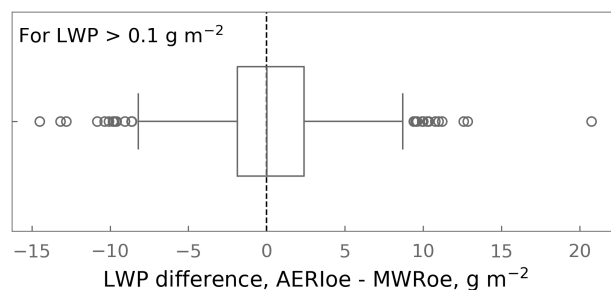


Figure 8. The differences in retrieved liquid water path (LWP) between all AERloe and MWRoe retrievals ($LWP > 0.1 \text{ g m}^{-2}$). 90% of all retrievals fall within the box plot ‘whiskers’, the remaining data are plotted as outliers (circles).

changes in LWP when the LWP is small, and so the 1σ uncertainty in the retrieved LWP from the AERloe is less than 1 g m^{-2} for $LWP < 20 \text{ g m}^{-2}$ (or less than 10%, Fig. 9). In contrast, the uncertainties in LWP derived from MWR brightness temperatures are related to absolute radiometric uncertainties that are approximately constant with respect to LWP, equating to at least 50% uncertainty for $LWP < 10 \text{ g m}^{-2}$ (Fig. 9). However, as the LWP approaches opacity in the infrared ($> 40 \text{ g m}^{-2}$) the sensitivity of the PAERI radiance observations to changes in LWP decreases until the uncertainties in the LWP retrievals from the AERloe become equivalent to those from the MWRoe ($\sim 3 \text{ g m}^{-2}$ or $\sim 6\%$ uncertainty at 50 g m^{-2}).

The high sensitivity of the AERloe to changes in LWP when LWP is small means that the increase in LWP associated with the development of radiation fog under clear skies is detected earlier in the AERloe retrievals compared to the MWRoe retrievals. The increased sensitivity of the infrared over the microwave to small LWP values was described in (Turner, 2007b). This is illustrated in Fig. 10, which shows the development of LWP during the 15 July 2019 case study. The AERloe LWP minus 2σ uncertainty increases to above 0.1 g m^{-2} shortly before 23 h on 15 July and continues to increase gradually, at a rate of $\sim 1.4 \text{ g m}^{-2} \text{ h}^{-1}$, until 02 h on 16 July, after which it increases rapidly to $\sim 30 \text{ g m}^{-2}$ at 03 h (Fig. 10). In contrast, due to the larger uncertainties in the MWRoe LWP retrieval, the MWRoe LWP does not increase to a value that is significantly different from the noise for at least 10 minutes until the onset of the rapid LWP increase just after 02 h. Despite the relatively

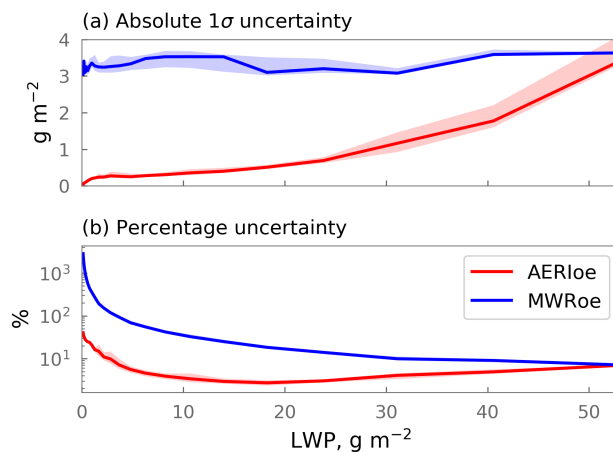


Figure 9. 1σ uncertainty in the AERloe (red) and MWRoe (blue) liquid water path (LWP) retrievals as a function of LWP. (a) Shows the absolute uncertainties and (b) shows the percentage uncertainties. The solid line is the median of all retrievals and shading is the interquartile range.

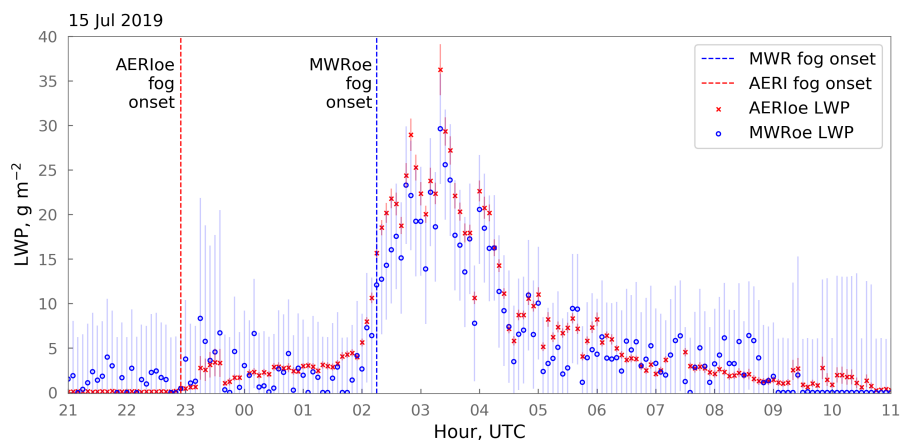


Figure 10. The evolution of fog liquid water path (LWP) during the 15 July 2019 case study retrieved from the AERloe (red) and the MWRoe (blue). Error bars show the 2σ uncertainty of the retrievals. The vertical red line shows the fog onset determined from the AERloe retrievals and the vertical blue line shows the fog onset determined by the MWRoe retrievals 3 hours later.

low LWP, the visibility at 00h was only 400 m and the observer reported freezing fog. In this case if the MWRoe LWP retrieval was used to detect fog or for visibility nowcasting, the fog at 00h on 16 July would not have been detected, whereas if the AERloe LWP retrieval was used instead, it would have been.

The AERloe retrieval consistently detects the onset of fog (via the increase in LWP) before the MWRoe retrieval (Fig. 11). Only for the 03 Aug case study does the MWRoe detect fog onset 30 minutes before the AERloe; for all other cases the

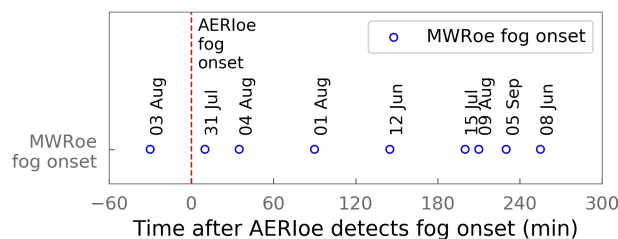


Figure 11. Time between fog onset detection from the AERIOe (vertical red line, $t=0$) and fog onset detection from the MWRoe for each fog case study where both sets of retrievals detected fog (blue circles). Note that for the 4 retrievals not included (13 July, 05 Aug, 14 Aug and 30 Sept), the MWRoe does not detect fog at all during the event whilst the AERIOe does.

AERIOe detects the fog before the MWRoe by up to 255 minutes (Fig. 11). In the four cases that are not shown on Fig. 11 (13 July, 05 Aug, 14 Aug and 30 Sept), the MWRoe never detects the fog whilst the AERIOe does. For all these cases where the
355 MWRoe does not detect the fog, the mean LWP detected by the AERIOe is very low ($< 2.5 \text{ g m}^{-2}$).

4 Discussion

Central Greenland provides an excellent opportunity to study climatologically relevant radiation fog due to the pristine environment, commonality of events, and presence of the ICECAPS long term multi-instrument platform. Nonetheless it is a unique environment and therefore the applicability of the results of this study in other environments is not guaranteed. Comparing retrievals between locations is complicated by the dependence on the quality of different prior datasets and instrument
360 calibrations. However, in general, the performance of the MWRoe and AERIOe thermodynamic profile retrievals in the lowest 1 km a.g.l are comparable to the performance assessed in a similar way against 127 radiosonde profiles in southwestern Germany (Blumberg et al., 2015). Blumberg et al. (2015) found the mean RMSE in the temperature profiles (lowest 1 km a.g.l) to be $\sim 0.9^\circ\text{C}$ for the AERIOe and $\sim 1.1^\circ\text{C}$ for the MWRoe (compared to 1.0°C and 1.6°C in this study), and for water
365 vapor profiles an RMSE of 0.7 g kg^{-1} for the AERIOe and 1.0 g kg^{-1} for the MWRoe (compared to 0.38 g kg^{-1} and 0.43 g kg^{-1} in this study). Nevertheless, under certain conditions, we might expect the performance of the AERIOe to deteriorate. For example, in environments where the total column water vapor is very high (e.g. tropical regions), the atmosphere will have a higher opacity in the infrared and the AERI sensitivity will be reduced (Löhnert et al., 2009). Additionally, the high sensitivity of the AERI, which makes it so suited to the study of fog, also makes it sensitive to localised plumes of pollution or smoke and
370 in some cases to atmospheric aerosols (e.g. Turner and Eloranta, 2008). Both sets of retrievals are also sensitive to the quality of the prior that is used to constrain the retrieval and provide a first guess (Turner and Löhnert, 2014), and to the calibration and characterisation of the particular instrument- which is typically more challenging for the MWR (see Appendix A, Blumberg et al., 2015, and Löhnert and Maier, 2012). All of these factors may impact performance at different locations and should be considered during experimental design. Note that neither instrument operates effectively in rain.



375 The radiation fog case studies presented in this study are all composed of supercooled water droplets, with some occurring
at surface temperatures as low as -27°C (table 3). Supercooled fogs at such cold temperatures are common at Summit, whereas
ice fogs during the summer are rare (Cox et al., 2019), and observations of ‘fog bows’ - atmospheric optics associated with
the scattering of light by liquid water droplets- during most case studies confirm the presence of liquid water. However, the
possibility exists that some (or even all) of these case studies contain ice crystals in addition to liquid water droplets. The
380 scattering and absorption properties of ice crystals can be quite different to those of water droplets at wavelengths that are
relevant for the AERIOe (e.g. Turner, 2005, Rowe et al., 2013), potentially resulting in biases in the AERIOe LWP retrievals
that assume a liquid only cloud. The lack of an independent ‘truth’ value for LWP means that we cannot quantify any such
biases. Nevertheless, the smaller uncertainties in the AERIOe LWP retrieval relative to the MWRoe LWP retrieval are related
to the physical sensitivity of the measurement, and so we can expect this result to be consistent across other cases of warm fog.

385 In this study, we do not use in-situ measurements of surface temperature and water vapor to constrain TROPoe, allowing
us to use these measurements as an independent ‘truth’ against which to evaluate the retrievals. However, it is possible to
include surface measurements in the TROPoe observation vector, and for operational purposes surface in-situ measurements
are typically used to constrain MWR thermodynamic profile retrievals (e.g. Cimini et al., 2015). . . . Results of Appendix B. . .

Previous studies have demonstrated that a combined instrument approach can provide optimal thermodynamic profile and
390 LWP retrievals throughout the boundary layer and under all-sky conditions (Turner et al., 2007a; Löhnert et al., 2009; Turner
and Löhnert, 2021; Smith et al., 2021; Djalalova et al., 2021). However, for the conditions relevant for the formation of radiation
fog (the near surface thermodynamic profile under clear skies or in the presence of optically thin fog) the performance of these
combined retrievals is equivalent to the performance of retrievals that only use AERI measurements. For this reason, we
do not consider a combined instrument approach in this study, however for multi-purpose applications that require accurate
395 near-surface retrievals in addition to above-cloud thermodynamic profiles, a combined instrument approach might provide the
optimal solution.

5 Summary and conclusions

Previous studies have demonstrated that AERI measurements of spectral infrared radiance are more sensitive to the structure of
the near-surface temperature profile and to small changes in liquid water path (LWP) than MWR measurements of microwave
400 brightness temperatures (Turner, 2007b; Löhnert et al., 2009; Blumberg et al., 2015). The purpose of this study was to compare
the results using a consistent physical retrieval algorithm (TROPoe) based on observations from the two instrument types during
cases of supercooled radiation fog in central Greenland (the AERIOe retrieval based on observations of infrared radiance and the
MWRoe based on microwave brightness temperatures). We assess the performance of the two retrievals against three criteria
that are critically important for the forecast and detection of radiation fog:

- 405 1. Ability to retrieve accurate thermodynamic profiles in the lowest 1 km a.g.l of the atmosphere.
2. Ability to capture the strength and development of shallow surface-based temperature inversions that typically portend
the formation of radiation fog.



3. Ability to detect the initial increase in LWP that signifies the onset of fog and a reduction in horizontal visibility.

Although there are only 16 coincident radiosonde profiles available for comparison, the bias and RMSE statistics of the
410 temperature and water vapor profiles in the lowest 1 km a.g.l are consistent with the findings of Löhnert et al. (2009) and
Blumberg et al. (2015), suggesting that the performance of both sets of retrievals in the Arctic and under conditions for the
formation of supercooled fog are similar to the performance in the mid-latitudes and under other sky conditions (clear skies
or below clouds with bases above 500 m a.g.l). We find that the water vapor profile retrievals in the lowest 1 km a.g.l are
comparable for both the MWRoe and the AERIOe with RMSE of 0.43 g kg^{-1} for the MWRoe and 0.38 g kg^{-1} for the
415 AERIOe. The AERIOe temperature profile retrievals perform better in terms of bias and RMSE than the MWRoe for the 16
cases considered (MWRoe bias: -1.5°C , RMSE: 1.6°C ; AERIOe bias: -0.45°C , RMSE: 1.0°C), however, the consistency of
the negative temperature bias in the MWRoe suggests that an additional bias correction may be possible that would result in
comparable performance between the two sets of retrievals.

A unique aspect of this study was the assessment of the ability of the two retrieval types to characterise shallow (0-10 m a.g.l)
420 surface-based temperature inversions. Despite the similar performance in general of the temperature profile retrievals up to 1 km
a.g.l, the ability of the two retrieval types to characterise the 0-10 m temperature lapse rate was markedly different. The AERIOe
0-10 m temperature differences were well correlated with in-situ observations, capturing surface temperature inversions well
up to a lapse rate of $-1.2^\circ\text{C m}^{-1}$ (previous studies have demonstrated the ability of the AERIOe to characterise near-surface
lapse rates well for values of -0.01 to $0.01^\circ\text{C m}^{-1}$, Klein et al., 2015). However, the MWRoe 0-10 m temperature differences
425 were not correlated with observations and did not deviate more than 1°C from the prior. The reason for this difference is that
the infrared radiance measurements from the AERI contain more information about the temperature near the surface than the
MWR measurements.

In addition to increased sensitivity to shallow surface temperature inversions, the AERI is much more sensitive to small
changes in LWP, with the result that the uncertainties in retrieved LWP from the AERIOe are much smaller than those retrieved
430 from the MWRoe for $\text{LWP} < 50 \text{ g m}^{-2}$. This means that the AERIOe is consistently able to detect small changes in LWP
that signify the onset of radiation fog and reduction in horizontal visibility by up to 255 minutes before the MWRoe. This has
important implications for fog detection and visibility nowcasting, because even a very small LWP ($< 5 \text{ g m}^{-2}$) can reduce
horizontal visibility, and the MWRoe alone would not have detected fog on some occasions when reported visibility was as
low as 400 m.

435 Based on these results, we hypothesise that the assimilation of near-surface temperature profile retrievals from an AERI
into NWP models could improve fog forecasts beyond the improvements already seen through the assimilation of MWR
measurements (Martinet et al., 2020). In addition, the increased sensitivity of the AERI to small changes in LWP (compared to
the MWR) will allow the AERI to detect fog onset earlier and miss fewer fog events, with the potential to increase the skill of
fog nowcasting products and improve climatological analyses of fog radiative effects. Although this study demonstrates that
440 the AERI is particularly well suited to retrieving boundary layer properties that are key for radiation fog formation, there are
trade-offs that must be considered when selecting instruments for operational use; notably that the AERI is unable to retrieve
thermodynamic profiles above optically thick clouds ($\text{LWP} > 40 \text{ g m}^{-2}$), and that the AERIOe retrieval is particularly sensitive



to the CBH assumption during fog / low cloud. The results of this study present a case for future observing system experiments (or observing system simulation experiments, for example as in Otkin et al., 2011; Hartung et al., 2011) to quantify the impact
445 of the operational use of AERI observations in terms of improvements to NWP skill, particularly in the case of radiation fog.

Data availability. ICECAPS data are available from the Arctic Data Center: HATPRO MWR (doi:10.18739/A2TX3568P), MMCR (doi:10.18739/A2Q52FD4V), POSS (doi:10.18739/A2GQ6R30G), and radiosonde profiles (doi:10.18739/A20P0WR53). PAERI data and retrieval output from the TROPoe are in the process of being submitted to the Arctic Data Center and are available upon request. ICECAPS-ACE HMP155 temperature/ humidity sensor data can be accessed through the CEDA archive at <http://catalogue.ceda.ac.uk/uuid/f06c6aa727404ca788ee3dd0515ea61a>.
450

Appendix A: MWR Tb bias correction

An external liquid nitrogen target is used to determine the effective temperature of the MWR internal noise diode, which is required to convert the observed signal into brightness temperature (Tb) values as described in section 2.1.2. Due to the personnel and resource requirements, this calibration is only performed twice a year at Summit. Imperfect calibrations can
455 result in a radiometric bias in the Tb measurements, and drift in the effective temperature of the internal noise diode can occur in between calibrations (Löhnert and Maier, 2012; Blumberg et al., 2015).

To determine this radiometric bias in the observed Tb values, the twice-daily radiosondes launched at Summit between 01 June and 31 August 2019 were used as input in the MonoRTM, and the bias between the observed and computed Tb values was determined. The evolution of the bias over time is well-illustrated by showing the bias values for the cases used in this analysis
460 (Fig A1). The bias in the K-band channels remained very small (absolute value less than 0.5 K), confirming that the automated tip curve calibration method applied to those transparent channels was working well. However, there is a significant negative bias (calculation larger than the observed radiance) in the 51 to 54 GHz channels, and this bias changes with time. However, the bias in the 51.26 and 52.28 GHz channels is variable with time with no apparent pattern (inset in Fig A1). Fortunately, the Tb bias in the 55 to 58 GHz channels is stable with time, and the magnitude is relatively small (less than 0.7 K for those
465 channels).

Note that we do not consider or correct for possible spectral biases in the MWR frequencies channels (Löhnert and Maier, 2012). It is possible that the large Tb biases in the 51.26, 52.28, and 53.86 GHz channels are a combination of both spectral and radiometric biases. It is important to note that the biases in those channels might not be entirely due to the calibration accuracy of the microwave radiometer; the bias could also be explained by systematic errors in the radiative transfer model used, as
470 the various uncertainties of the absorption line properties at those frequencies results in large model uncertainty (Cimini et al., 2018).

Figure A2 illustrates the difference between the MWR_{oe}-retrieved thermodynamic profile compared to the radiosondes during the radiation fog case studies with and without the mean radiosonde-derived bias correction applied. The application of the bias correction reduces the mean bias in the water vapor profile from 0.14 g kg⁻¹ to 0.01 g kg⁻¹ and the mean RMSE

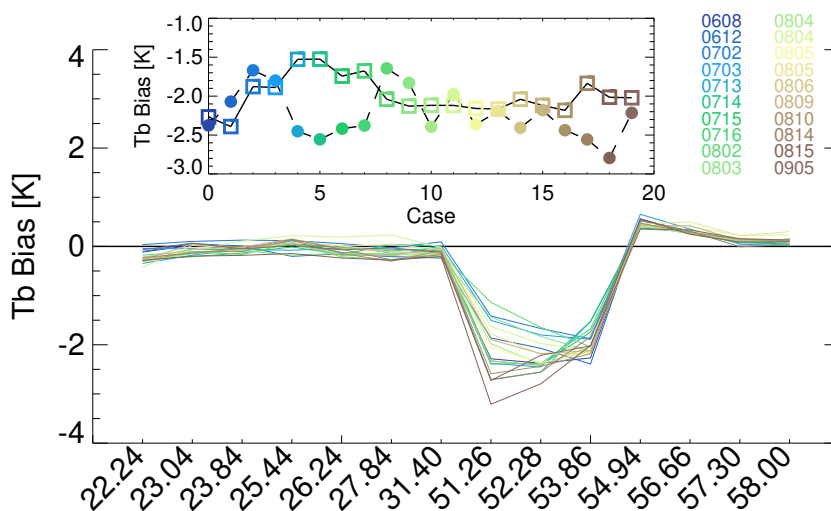


Figure A1. The Tb bias offset for the cases used in this analysis. The inset plot shows the temporal variability of the 51.26 (filled circles) and 52.28 (open squares) GHz channels for these cases, where the colors indicate the date (MMDD) of the case.

475 from 0.47 g kg^{-1} to 0.43 g kg^{-1} . However, the bias correction has little effect on the temperature profiles. The reason for the consistent small negative temperature bias in the MWRoe both with (mean $-1.45 \text{ }^\circ\text{C}$) and without (mean $-1.26 \text{ }^\circ\text{C}$) the bias correction is currently unknown, especially since the mean Tb bias in the high-frequency end of the V-band is very close to zero.

480 The reduction in the bias and RMSE of the MWRoe-retrieved water vapor profile compared to the radiosondes demonstrates that the application of the additional Tb bias correction is essential for making accurate MWR thermodynamic profile retrievals. Currently the only way of performing this bias correction is by using an alternative ‘truth’ profile (in this case radiosonde profiles); this is a significant disadvantage of the MWR since radiosondes are spatially sparse, resource intensive, and expensive. However, a method using only the climatology data, as encapsulated in the a priori data, has been proposed by Djalalova et al. (2021); this new method helps to account for some of the spectral artifacts in the bias but needs additional research to help
 485 characterize any systematic error that might be introduced by the method.

Appendix B: The impact of constraining the retrievals by surface meteorological data.

Operational retrievals of thermodynamic profiles from MWRs are typically constrained by an in-situ measurement of surface temperature, usually from a sensor that is integrated with the MWR (e.g. Cimini et al., 2015). We did not include this constraint in the TROPoe retrievals (either AERI- or MWR-based) to allow for the use of the in-situ surface temperature as an independent validation measurement. To illustrate the impact of including the in-situ surface temperature in the MWR retrieval, we ran
 490 another set of retrievals (MWRoe-sfc) which is identical to the MWRoe except that it includes the in-situ surface temperature

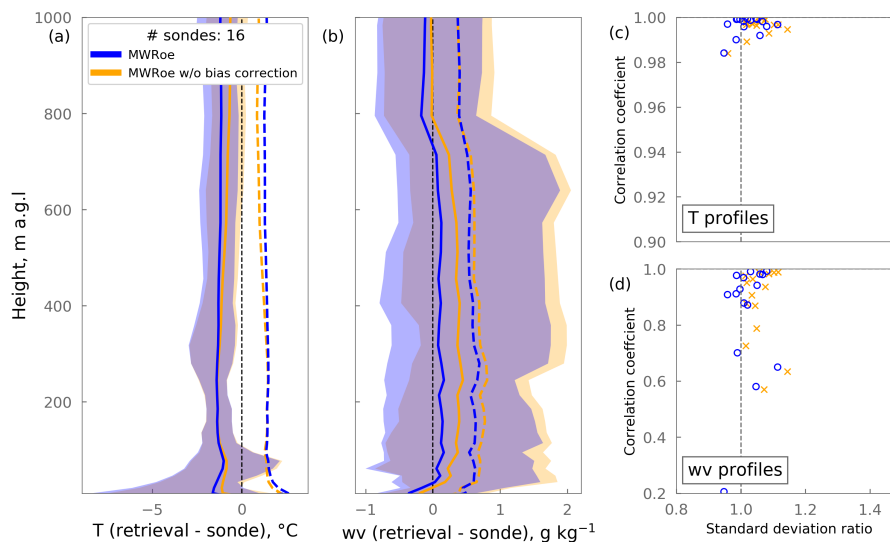


Figure A2. As figure 4 but comparing the performance of the final MWRoe retrieval (blue) with that of the MWRoe retrieval without the additional T_b bias correction applied (orange). The solid line shows the mean bias and the shaded represents the range. Dashed lines show the root mean squared error (RMSE).

and water vapour observation from the HMP155 sensor in the observation vector. Since the microwave brightness temperatures contain very little information about the surface temperature (Fig. 7), the additional constraint dominates the surface temperature retrieval so that the ‘retrieved’ surface temperature from the MWRoe-sfc is essentially the same as the in-situ temperature measurement (Fig. B1a). By aligning the MWRoe-sfc surface temperature with the in-situ measurement, the representation of the surface temperature inversion defined as the difference between the 10 m and surface temperature is naturally improved. However, note that the 10 m temperatures retrieved by the MWRoe-sfc perform only marginally better than that of the MWRoe compared to the 10 m in-situ measurement, and not as well as the AERIOe which did not include the extra information from the in-situ surface temperature probe (Fig. B1b). This implies that constraining the retrieval by the in-situ surface temperature does not translate to improvements in the temperature profile retrieval above that level.

Figure B2 shows that the mean degrees of freedom for signal for the surface temperature retrieval is over four times higher for the MWRoe-sfc compared to the MWRoe due to the additional information about the surface temperature in the observation vector. However, above the surface, the AERIOe still contains more information about the temperature profile than the MWRoe-sfc in the lowest 500 m of the boundary layer; the region in which accurate temperature profiles in NWP models are critical for successful fog forecasts (Martinet et al., 2020).

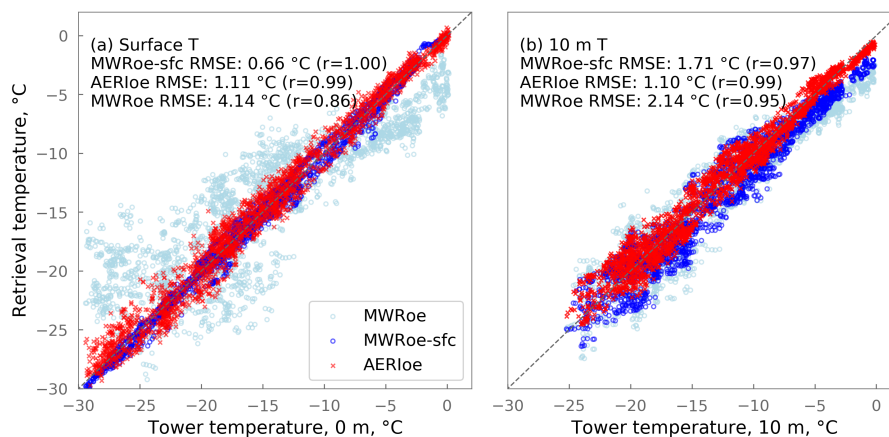


Figure B1. Retrieved temperature versus in-situ measurements from the tower at the surface (a) and 10 m (b). The MWRoe retrievals used in the main study are plotted in pale blue, the AERloe retrievals in red, and the MWRoe retrievals that are constrained by the surface temperature (MWRoe-sfc) are in blue.

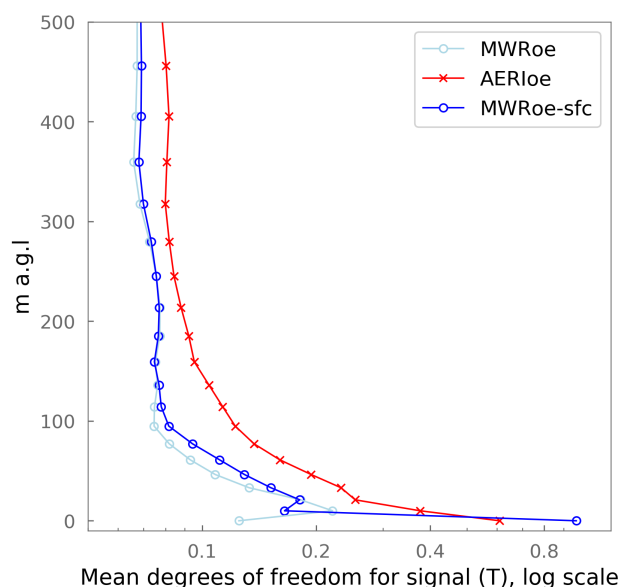


Figure B2. Mean degrees of freedom for signal across all temperature retrievals from the MWRoe (pale blue), the AERloe (red), and the MWRoe constrained by the in-situ surface temperature measurement, MWRoe-sfc (blue).

Author contributions. DT conceived the study, developed and ran the TROPoe retrieval algorithm, processed the MWR data, calculated the T_b bias correction, and contributed to the text. VW prepared the PAERI data and contributed to the text. HG led the analysis with contributions from DT and RN. HG prepared the manuscript with contributions from all co-authors.



Competing interests. The authors declare that they have no conflict of interest.

510 *Acknowledgements.* The efforts of technicians at Summit Station and science support provided by Polar Field Services were crucial to main-
taining data quality and continuity at Summit. ICECAPS is a long-term research program with many collaborators, and we are grateful for
all their efforts in developing and maintaining the various instruments and data products used in this study. Financial support for ICECAPS-
ACE was provided by NSFGE0-NERC grant 1801477, and HG was funded by the NERC SPHERES DTP grant number NE/L002574/1. We
would like to thank Maria Cadeddu, Argonne National Laboratory, for her work in updating the HATPRO's calibration using automated tip
515 curves. Finally we are grateful for feedback from the PROBE-COST fog alerts meeting (23 Nov 2021) that improved this manuscript.



References

- Anber, U., Gentine, P., Wang, S., and Sobel, A. H.: Fog and rain in the Amazon, *Proceedings of the National Academy of Sciences*, 112, 11 473–11 477, 2015.
- Antonelli, P., Revercomb, H., Sromovsky, L., Smith, W., Knuteson, R., Tobin, D., Garcia, R., Howell, H., Huang, H.-L., and Best, F.: A
520 principal component noise filter for high spectral resolution infrared measurements, *Journal of Geophysical Research: Atmospheres*, 109, 2004.
- Beiderwieden, E., Klemm, O., and Hsia, Y. J.: The impact of fog on the energy budget of a subtropical cypress forest in Taiwan, Taiwan
Journal of Forest Science, 22, 227–239, <https://doi.org/10.7075/TJFS.200709.0227>, 2007.
- Bendix, J.: A case study on the determination of fog optical depth and liquid water path using AVHRR data and relations to fog
525 liquid water content and horizontal visibility A case study on the determination of fog optical depth and liquid water path using AVHRR data and relations to fog liquid water content and horizontal visibility, *INT. J. REMOTE SENSING*, 16, 515–530, <https://doi.org/10.1080/01431169508954416>, 1995.
- Bennartz, R., Shupe, M. D., Turner, D. D., Walden, V. P., Steffen, K., Cox, C. J., Kulie, M. S., Miller, N. B., and Pettersen, C.: July 2012
Greenland melt extent enhanced by low-level liquid clouds, *Nature*, 496, 83, <https://doi.org/10.1038/nature12002>, 2013.
- 530 Bergot, T., Terradellas, E., Cuxart, J., Mira, A., Liechti, O., Mueller, M., and Nielsen, N. W.: Intercomparison of Single-Column Numerical Models for the Prediction of Radiation Fog, *Journal of Applied Meteorology and Climatology*, 46, 504–521, <https://doi.org/10.1175/JAM2475.1>, 2007.
- Blumberg, W. G., Turner, D. D., Löhnert, U., and Castleberry, S.: Ground-Based Temperature and Humidity Profiling Using Spectral Infrared and Microwave Observations. Part II: Actual Retrieval Performance in Clear-Sky and Cloudy Conditions, *Journal of Applied Meteorology and Climatology*, 54, 2305–2319, <https://doi.org/10.1175/JAMC-D-15-0005.1>, 2015.
- 535 Cadeddu, M. P., Liljegren, J. C., and Turner, D. D.: The Atmospheric radiation measurement (ARM) program network of microwave radiometers: instrumentation, data, and retrievals, *Atmos. Meas. Tech*, 6, 2359–2372, <https://doi.org/10.5194/amt-6-2359-2013>, 2013.
- Cao, Y., Tan, W., and Wu, Z.: Aircraft icing: An ongoing threat to aviation safety, *Aerospace science and technology*, 75, 353–385, 2018.
- Cimini, D., Nelson, M., Güldner, J., and Ware, R.: Forecast indices from a ground-based microwave radiometer for operational meteorology,
540 *Atmospheric Measurement Techniques*, 8, 315–333, <https://doi.org/10.5194/AMT-8-315-2015>, 2015.
- Cimini, D., Rosenkranz, P. W., Tretyakov, M. Y., Koshelev, M. A., and Romano, F.: Uncertainty of atmospheric microwave absorption model: impact on ground-based radiometer simulations and retrievals, *Atmospheric Chemistry and Physics*, 18, 15 231–15 259, <https://doi.org/10.5194/acp-18-15231-2018>, 2018.
- Clough, S., Shephard, M., Mlawer, E., Delamere, J., Iacono, M., Cady-Pereira, K., Boukabara, S., and Brown, P.: Atmospheric radiative
545 transfer modeling: A summary of the AER codes, *Journal of Quantitative Spectroscopy and Radiative Transfer*, 91, 233–244, 2005.
- Clough, S. A. and Iacono, M. J.: Line-by-line calculation of atmospheric fluxes and cooling rates: 2. Application to carbon dioxide, ozone, methane, nitrous oxide and the halocarbons, *Journal of Geophysical Research: Atmospheres*, 100, 16 519–16 535, <https://doi.org/10.1029/95JD01386>, 1995.
- Cox, C. J., Walden, V. P., and Rowe, P. M.: A comparison of the atmospheric conditions at Eureka, Canada, and Barrow, Alaska (2006–2008),
550 *Journal of Geophysical Research: Atmospheres*, 117, 2012.



- Cox, C. J., Noone, D. C., Berkelhammer, M., Shupe, M. D., Neff, W. D., Miller, N. B., Walden, V. P., and Steffen, K.: Supercooled liquid fogs over the central Greenland Ice Sheet, *Atmospheric Chemistry and Physics*, 19, 7467–7485, <https://doi.org/10.5194/acp-19-7467-2019>, 2019.
- Crewell, S. and Lohnert, U.: Accuracy of Boundary Layer Temperature Profiles Retrieved with Multi-frequency, Multiangle Microwave Radiometry, *SPECIAL ISSUE ON MICROWAVE RADIOMETRY AND REMOTE SENSING APPLICATIONS*, 2007.
- 555 Djalalova, I. V., Turner, D. D., Bianco, L., Wilczak, J. M., Duncan, J., Adler, B., and Gottas, D.: Improving thermodynamic profile retrievals from microwave radiometers by including Radio Acoustic Sounding System (RASS) observations, *Atmospheric Measurement Techniques Discussions*, pp. 1–50, 2021.
- Ducloux, H. and Nygaard, B. E.: Ice loads on overhead lines due to freezing radiation fog events in plains, *Cold Regions Science and Technology*, 153, 120–129, <https://doi.org/10.1016/J.COLDREGIONS.2018.04.018>, 2018.
- 560 Gultepe, I., Tardif, R., Michaelides, S. C., Cermak, J., Bott, A., Bendix, J., Müller, M. D., Pagowski, M., Hansen, B., Ellrod, G., Jacobs, W., Toth, G., and Cober, S. G.: Fog research: A review of past achievements and future perspectives, <https://doi.org/10.1007/s00024-007-0211-x>, 2007.
- Gultepe, I., Pearson, G., Milbrandt, J. A., Hansen, B., Platnick, S., Taylor, P., Gordon, M., Oakley, J. P., and Cober, S. G.: The Fog Remote Sensing and Modeling Field Project, *Bulletin of the American Meteorological Society*, 90, 341–360, <https://doi.org/10.1175/2008BAMS2354.1>, 2009.
- 565 Gultepe, I., Sharman, R., Williams, P. D., Zhou, B., Ellrod, G., Minnis, P., Trier, S., Griffin, S., Yum, S. S., and Gharabaghi, B.: A Review of High Impact Weather for Aviation Meteorology, *Pure and Applied Geophysics*, 176, 18, <https://doi.org/10.1007/s00024-019-02168-6>, 2019.
- 570 Guy, H., Neely III, R. R., and Brooks, I.: ICECAPS-ACE: Integrated Characterization of Energy, Clouds, Atmospheric state, and Precipitation at Summit, Greenland - Aerosol Cloud Experiment measurements., Centre for Environmental Data Analysis, <http://catalogue.ceda.ac.uk/uuid/f06c6aa727404ca788ee3dd0515ea61a>, 2020.
- Guy, H., Brooks, I., Carslaw, K., Murray, B., Walden, V., Shupe, M., Pettersen, C., Turner, D., Cox, C., Neff, W., Bennartz, R., and Neely III, R.: Controls on surface aerosol number concentrations and aerosol-limited cloud regimes over the central Greenland Ice Sheet, *Atmospheric Chemistry and Physics*, pp. 1–36, <https://doi.org/10.5194/acp-2021-491>, 2021.
- 575 Hachfeld, B., Jürgens, N., et al.: Climate patterns and their impact on the vegetation in a fog driven desert: the Central Namib Desert in Namibia., *Phytocoenologia*, 30, 567–589, 2000.
- Han, Y.: Analysis and improvement of tipping calibration for ground-based microwave radiometers, *IEEE Transactions on Geoscience and Remote Sensing*, 38, 1260–1276, <https://doi.org/10.1109/36.843018>, 2000.
- 580 Hartung, D. C., Otkin, J. A., Petersen, R. A., Turner, D. D., and Feltz, W. F.: Assimilation of Surface-Based Boundary Layer Profiler Observations during a Cool-Season Weather Event Using an Observing System Simulation Experiment. Part II: Forecast Assessment, *Monthly Weather Review*, 139, 2327–2346, <https://doi.org/10.1175/2011MWR3623.1>, 2011.
- Hudson, S. R. and Brandt, R. E.: A look at the surface-based temperature inversion on the Antarctic Plateau, *Journal of Climate*, 18, 1673–1696, 2005.
- 585 Illingworth, A. J., Cimini, D., Haefele, A., Haeffelin, M., Hervo, M., Kotthaus, S., Löhnert, U., Martinet, P., Mattis, I., O'Connor, E. J., and Potthast, R.: How Can Existing Ground-Based Profiling Instruments Improve European Weather Forecasts?, *Bulletin of the American Meteorological Society*, 100, 605–619, <https://doi.org/10.1175/BAMS-D-17-0231.1>, 2019.



- Izett, J. G., Schilperoord, B., Coenders-Gerrits, M., Baas, P., Bosveld, F. C., and van de Wiel, B. J. H.: Missed Fog?, *Boundary-Layer Meteorology* 2019 173:2, 173, 289–309, <https://doi.org/10.1007/S10546-019-00462-3>, 2019.
- 590 Jacob, J. D., Chilson, P. B., Houston, A. L., and Smith, S. W.: Considerations for atmospheric measurements with small unmanned aircraft systems, *Atmosphere*, 9, 252, 2018.
- Jensen, M. P., Holdridge, D. J., Survo, P., Lehtinen, R., Baxter, S., Toto, T., and Johnson, K. L.: Comparison of Vaisala radiosondes RS41 and RS92 at the ARM Southern Great Plains site, *Atmospheric Measurement Techniques*, 9, 3115–3129, 2016.
- Klein, P., Bonin, T. A., Newman, J. F., Turner, D. D., Chilson, P. B., Wainwright, C. E., Blumberg, W. G., Mishra, S., Carney, M., Jacacobsen,
595 E. P., Wharton, S., and Newsom, R. K.: LABEL: A Multi-Institutional, Student-Led, Atmospheric Boundary Layer Experiment, *Bulletin of the American Meteorological Society*, 96, 1743–1764, <https://doi.org/10.1175/BAMS-D-13-00267.1>, 2015.
- Knuteson, R., Revercomb, H., Best, F., Ciganovich, N., Dedecker, R., Dirx, T., Ellington, S., Feltz, W., Garcia, R., Howell, H., et al.: Atmospheric emitted radiance interferometer. Part I: Instrument design, *Journal of Atmospheric and Oceanic Technology*, 21, 1763–1776, 2004a.
- 600 Knuteson, R., Revercomb, H., Best, F., Ciganovich, N., Dedecker, R., Dirx, T., Ellington, S., Feltz, W., Garcia, R., Howell, H., et al.: Atmospheric emitted radiance interferometer. Part I: Instrument design, *Journal of Atmospheric and Oceanic Technology*, 21, 1763–1776, 2004b.
- Koenigk, T., Key, J., and Vihma, T.: Climate change in the Arctic, in: *Physics and chemistry of the Arctic atmosphere*, pp. 673–705, Springer, 2020.
- 605 Liljegren, J. C.: Automatic self-calibration of ARM microwave radiometers, *Microwave Radiometry and Remote Sensing of the Earth's Surface and Atmosphere*, 433, 433–443, 2000.
- Löhnert, U. and Maier, O.: Operational profiling of temperature using ground-based microwave radiometry at Payerne: Prospects and challenges, *Atmospheric Measurement Techniques*, 5, 1121–1134, <https://doi.org/10.5194/AMT-5-1121-2012>, 2012.
- Löhnert, U., Turner, D. D., and Crewell, S.: Ground-Based Temperature and Humidity Profiling Using Spectral Infrared and Microwave
610 Observations. Part I: Simulated Retrieval Performance in Clear-Sky Conditions, *Journal of Applied Meteorology and Climatology*, 48, 1017–1032, <https://doi.org/10.1175/2008JAMC2060.1>, 2009.
- Martinet, P., Cimini, D., De Angelis, F., Canut, G., Unger, V., Guillot, R., Tzanos, D., and Paci, A.: Combining ground-based microwave radiometer and the AROME convective scale model through 1DVAR retrievals in complex terrain: An Alpine valley case study, *Atmospheric Measurement Techniques*, 10, 3385–3402, <https://doi.org/10.5194/AMT-10-3385-2017>, 2017.
- 615 Martinet, P., Cimini, D., Burnet, F., Ménérier, B., Michel, Y., and Unger, V.: Improvement of numerical weather prediction model analysis during fog conditions through the assimilation of ground-based microwave radiometer observations: A 1D-Var study, *Atmospheric Measurement Techniques*, 13, 6593–6611, <https://doi.org/10.5194/AMT-13-6593-2020>, 2020.
- McFarquhar, G. M., Smith, E., Pillar-Little, E. A., Brewster, K., Chilson, P. B., Lee, T. R., Waugh, S., Yussouf, N., Wang, X., Xue, M., et al.: Current and future uses of UAS for improved forecasts/warnings and scientific studies, *Bulletin of the American Meteorological Society*,
620 101, E1322–E1328, 2020.
- Miller, N. B., Shupe, M. D., Cox, C. J., Walden, V. P., Turner, D. D., and Steffen, K.: Cloud radiative forcing at Summit, Greenland, *Journal of Climate*, 28, 6267–6280, 2015.
- Moran, K. P., Martner, B. E., Post, M., Kropfli, R. A., Welsh, D. C., and Widener, K. B.: An unattended cloud-profiling radar for use in climate research, *Bulletin of the American Meteorological Society*, 79, 443–456, 1998.
- 625 Morris, V. R.: Ceilometer instrument handbook, DOE Office of Science Atmospheric Radiation Measurement (ARM) User Facility, 2016.



- Münel, C., Eresmaa, N., Räsänen, J., and Karppinen, A.: Retrieval of mixing height and dust concentration with lidar ceilometer, *Boundary-Layer Meteorology* 2006 124:1, 124, 117–128, <https://doi.org/10.1007/S10546-006-9103-3>, 2006.
- Newsom, R. K., Turner, D. D., Lehtinen, R., Münel, C., Kallio, J., and Roininen, R.: Evaluation of a Compact Broadband Differential Absorption Lidar for Routine Water Vapor Profiling in the Atmospheric Boundary Layer, *Journal of Atmospheric and Oceanic Technology*, 630 37, 47–65, <https://doi.org/10.1175/JTECH-D-18-0102.1>, 2020.
- NSIDC: Europe’s warm air spikes Greenland melting to record levels., National Snow and Ice Data Center, <http://nsidc.org/greenland-today/2021/08/rain-at-the-summit-of-greenland/>, 2019.
- NSIDC: Rain at the summit of Greenland., National Snow and Ice Data Center, <http://nsidc.org/greenland-today/2021/08/rain-at-the-summit-of-greenland/>, 2021.
- 635 Oke, T. R.: *Boundary layer climates*, Routledge, 2002.
- Otkin, J. A., Hartung, D. C., Turner, D. D., Petersen, R. A., Feltz, W. F., and Janzon, E.: Assimilation of Surface-Based Boundary Layer Profiler Observations during a Cool-Season Weather Event Using an Observing System Simulation Experiment. Part I: Analysis Impact, *Monthly Weather Review*, 139, 2309–2326, <https://doi.org/10.1175/2011MWR3622.1>, 2011.
- Panahi, R., Ng, A. K., Afenyo, M. K., and Haeri, F.: A novel approach in probabilistic quantification of risks within the context of maritime 640 supply chain: The case of extreme weather events in the Arctic, *Accident Analysis & Prevention*, 144, 105 673, 2020.
- Price, J.: Radiation Fog. Part I: Observations of Stability and Drop Size Distributions, *Boundary-Layer Meteorology* 2011 139:2, 139, 167–191, <https://doi.org/10.1007/S10546-010-9580-2>, 2011.
- Rodgers, C. D.: *Inverse methods for atmospheric sounding: theory and practice*, vol. 2, World scientific, 2000.
- Rose, T., Crewell, S., Löhnert, U., and Simmer, C.: A network suitable microwave radiometer for operational monitoring of the cloudy 645 atmosphere, *Atmospheric Research*, 75, 183–200, <https://doi.org/10.1016/j.atmosres.2004.12.005>, 2005.
- Rowe, P. M., Neshyba, S., and Walden, V.: Radiative consequences of low-temperature infrared refractive indices for supercooled water clouds, *Atmospheric Chemistry and Physics*, 13, 11 925–11 933, 2013.
- Rüfenacht, R., Haefele, A., Pospichal, B., Cimini, D., Bircher-Adrot, S., Turp, M., and Sugier, J.: EUMETNET opens to microwave radiometers for operational thermodynamical profiling in Europe, *Bulletin of Atmospheric Science and Technology* 2021 2:1, 2, 1–5, 650 <https://doi.org/10.1007/S42865-021-00033-W>, 2021.
- Savijärvi, H.: Radiative and turbulent heating rates in the clear-air boundary layer, *Quarterly Journal of the Royal Meteorological Society*, 132, 147–161, <https://doi.org/10.1256/QJ.05.61>, 2006.
- Sheppard, B. and Joe, P.: Performance of the precipitation occurrence sensor system as a precipitation gauge, *Journal of Atmospheric and Oceanic Technology*, 25, 196–212, 2008.
- 655 Shupe, M. D. and Intrieri, J. M.: Cloud radiative forcing of the Arctic surface: The influence of cloud properties, surface albedo, and solar zenith angle, *Journal of Climate*, 17, 616–628, 2004.
- Shupe, M. D., Turner, D. D., Walden, V. P., Bennartz, R., Cadeddu, M. P., Castellani, B. B., Cox, C. J., Hudak, D. R., Kulie, M. S., Miller, N. B., Neely, R. R., Neff, W. D., Rowe, P. M., Others, Neely, R. R., Neff, W. D., and Rowe, P. M.: High and dry: New observations of tropospheric and cloud properties above the Greenland Ice Sheet, *Bulletin of the American Meteorological Society*, 94, 169–186, 660 <https://doi.org/10.1175/BAMS-D-11-00249.1>, 2013.
- Smith, E. N., Greene, B. R., Bell, T. M., Blumberg, W. G., Wakefield, R., Reif, D., Niu, Q., Wang, Q., and Turner, D. D.: Evaluation and Applications of Multi-Instrument Boundary-Layer Thermodynamic Retrievals, *Boundary-Layer Meteorology* 2021 181:1, 181, 95–123, <https://doi.org/10.1007/S10546-021-00640-2>, 2021.



- Solomon, A., Shupe, M. D., and Miller, N. B.: Cloud–atmospheric boundary layer–surface interactions on the Greenland Ice Sheet during the July 2012 extreme melt event, *Journal of Climate*, 30, 3237–3252, 2017.
- 665 Steeneveld, G. J., Ronda, R. J., and Holtslag, A. A. M.: The Challenge of Forecasting the Onset and Development of Radiation Fog Using Mesoscale Atmospheric Models, *Boundary-Layer Meteorology* 2014 154:2, 154, 265–289, <https://doi.org/10.1007/S10546-014-9973-8>, 2014.
- Stillwell, R. A., Spuler, S. M., Hayman, M., Repasky, K. S., and Bunn, C. E.: Demonstration of a combined differential absorption and high spectral resolution lidar for profiling atmospheric temperature, *Optics express*, 28, 71–93, 2020.
- 670 Tardif, R.: The impact of vertical resolution in the explicit numerical forecasting of radiation fog: A case study, in: *Fog and boundary layer clouds: Fog visibility and forecasting*, pp. 1221–1240, Springer, 2007.
- Taylor, K. E.: Summarizing multiple aspects of model performance in a single diagram, *Journal of Geophysical Research: Atmospheres*, 106, 7183–7192, <https://doi.org/10.1029/2000JD900719>, 2001.
- 675 Temimi, M., Fonseca, R. M., Nelli, N. R., Valappil, V. K., Weston, M. J., Thota, M. S., Wehbe, Y., and Yousef, L.: On the analysis of ground-based microwave radiometer data during fog conditions, *Atmospheric Research*, 231, 104652, <https://doi.org/10.1016/J.ATMOSRES.2019.104652>, 2020.
- Turner, D., Knuteson, R., Revercomb, H., Lo, C., and Dedecker, R.: Noise reduction of Atmospheric Emitted Radiance Interferometer (AERI) observations using principal component analysis, *Journal of Atmospheric and Oceanic Technology*, 23, 1223–1238, 2006.
- 680 Turner, D. D.: Arctic mixed-phase cloud properties from AERI lidar observations: Algorithm and results from SHEBA, *Journal of Applied Meteorology*, 44, 427–444, <https://doi.org/10.1175/JAM2208.1>, 2005.
- Turner, D. D.: Improved ground-based liquid water path retrievals using a combined infrared and microwave approach, *Journal of Geophysical Research: Atmospheres*, 112, 15 204, <https://doi.org/10.1029/2007JD008530>, 2007b.
- Turner, D. D. and Blumberg, W. G.: Improvements to the AERIOe thermodynamic profile retrieval algorithm, *IEEE Journal of Selected Topics in Applied Earth Observations and Remote Sensing*, 12, 1339–1354, <https://doi.org/10.1109/JSTARS.2018.2874968>, 2019.
- 685 Turner, D. D. and Eloranta, E. W.: Validating mixed-phase cloud optical depth retrieved from infrared observations with high spectral resolution lidar, *IEEE Geoscience and Remote Sensing Letters*, 5, 285–288, <https://doi.org/10.1109/LGRS.2008.915940>, 2008.
- Turner, D. D. and Löhnert, U.: Information Content and Uncertainties in Thermodynamic Profiles and Liquid Cloud Properties Retrieved from the Ground-Based Atmospheric Emitted Radiance Interferometer (AERI), *Journal of Applied Meteorology and Climatology*, 53, 752–771, <https://doi.org/10.1175/JAMC-D-13-0126.1>, 2014.
- 690 Turner, D. D. and Löhnert, U.: Ground-based temperature and humidity profiling: Combining active and passive remote sensors, *Atmospheric Measurement Techniques*, 14, 3033–3048, <https://doi.org/10.5194/AMT-14-3033-2021>, 2021.
- Turner, D. D., Vogelmann, A., Austin, R. T., Barnard, J. C., Cady-Pereira, K., Chiu, J. C., Clough, S. A., Flynn, C., Khaiyer, M. M., Liljegren, J., et al.: Thin liquid water clouds: Their importance and our challenge, *Bulletin of the American Meteorological Society*, 88, 177–190, 2007a.
- 695 Turner, D. D., Kneifel, S., and Cadetdu, M. P.: An Improved Liquid Water Absorption Model at Microwave Frequencies for Supercooled Liquid Water Clouds, *Journal of Atmospheric and Oceanic Technology*, 33, 33–44, <https://doi.org/10.1175/JTECH-D-15-0074.1>, 2016.
- Wærsted, E. G., Haeffelin, M., Dupont, J. C., Delanoë, J., and Dubuisson, P.: Radiation in fog: Quantification of the impact on fog liquid water based on ground-based remote sensing, *Atmospheric Chemistry and Physics*, 17, 10 811–10 835, <https://doi.org/10.5194/ACP-17-10811-2017>, 2017.
- 700



- Walden, V., Town, M., Halter, B., and Storey, J.: First measurements of the infrared sky brightness at Dome C, Antarctica, *Publications of the Astronomical Society of the Pacific*, 117, 300, 2005.
- Westerhuis, S. and Fuhrer, O.: A Locally Smoothed Terrain-Following Vertical Coordinate to Improve the Simulation of Fog and Low Stratus in Numerical Weather Prediction Models, *Journal of Advances in Modeling Earth Systems*, 13, e2020MS002437, <https://doi.org/10.1029/2020MS002437>, 2021.
- 705
- Wilcox, E. M.: Multi-spectral Remote Sensing of Sea Fog with Simultaneous Passive Infrared and Microwave Sensors, pp. 511–526, https://doi.org/10.1007/978-3-319-45229-6_11, 2017.
- Wu, D., Lu, B., Zhang, T., and Yan, F.: A method of detecting sea fogs using CALIOP data and its application to improve MODIS-based sea fog detection, *Journal of Quantitative Spectroscopy and Radiative Transfer*, 153, 88–94, <https://doi.org/10.1016/J.QSRT.2014.09.021>, 710 2015.
- Wulfmeyer, V., Hardesty, R. M., Turner, D. D., Behrendt, A., Cadeddu, M. P., Girolamo, P. D., Schlüssel, P., Baelen, J. V., and Zus, F.: A review of the remote sensing of lower tropospheric thermodynamic profiles and its indispensable role for the understanding and the simulation of water and energy cycles, *Reviews of Geophysics*, 53, 819–895, <https://doi.org/10.1002/2014RG000476>, 2015.
- Yi, L., Li, K.-F., Chen, X., and Tung, K.-K.: Arctic Fog Detection Using Infrared Spectral Measurements, *Journal of Atmospheric and Oceanic Technology*, 36, 1643–1656, <https://doi.org/10.1175/JTECH-D-18-0100.1>, 2019.
- 715